The effect of point defects on irradiation damage of Fe-based composite materials for fusion reactor

Jingming Shi

Graduate School of Engineering

Hokkaido University

Published Work

- "Study on synergistic effects of H and He in α-Fe", Jingming Shi, Naoyuki Hashimoto, Nuclear Materials and Energy 16 (2018) 212-216.

- "Doping of Interstitials (H, He, C, N) in CrCoFeNi High Entropy Alloy: A DFT Study", Jingming Shi, Yu Lei, Naoyuki Hashimoto, Shigehito Isobe, Materials Transactions 61 (2020) 616-621.

- "Behavior of hydrogen at Fe/W interface: a first principle calculation study", Jingming Shi, Naoyuki Hashimoto, Shigehito Isobe, Journal of Nulcear Science and Technology, (2020), 1-8.

- "Cohesion properties of incoherent Fe/W interfaces: A DFT study", Jingming Shi, Naoyuki Hashimoto, Shigehito Isobe, Journal of Nulcear Materials, Under review.

- "Highly Correlated Size and Composition of Pt/Au Alloy Nanoparticles via Magnetron Sputtering onto Liquid", Deng LL, Nguyen MT, Shi JM, Chau YTR, Tokunaga T, Kudo M, Matsumura S, Hashimoto N, Yonezawa T, Langmuir, 36 (2020) 3004-3015.

Awards

- Best Poster Award

  The Nineteenth International Conference on Fusion Reactor Materials (ICFRM-18), October 27 – November 1, 2019, La Jolla, California, U.S.A.

Acknowledgement

It has been four years, since I came to Japan to persuade the degree in materials science and engineering. Now my study is going to the end. At this moment, I would like to acknowledge and give thanks to the following people. PhD course is really a challenge for me, I couldn't have the chance to finish it without their support and help.

Professor Naoyuki Hashimoto

Prof. Hashimoto accepted me as his doctoral student, even though I didn't have a irradiation related background. I am extremely grateful to have the chance to study at his lab under his guidance. He gave me a lot of support on my research by discussing with me about the research and giving me very helpful advises. Also, he gave a lot of help on my life. I really learned a lot and really enjoyed the life in lab. I need to say thank you very much to him, but I also want to say sorry for him. Since I am not a typical PhD student, I'm sorry for the inconvenience I caused.

Professor Shigehito Isobe

Prof. Isobe is not my supervisor, but he also gave me a lot support. We discussed about research and also about the things which is not about research. I enjoyed the discussion with him.

Professor Somei Ohnuki

I need to give my special thanks to Prof. Ohnuki. I met with him at 2010 for the first time. Without him, I would not have the idea of studying abroad. I got his help before and after I came to Japan. He took me to many places and tought me a lot of things includes research and Japanese culture. I really enjoyed the time with him.

Ms. Kaori Kobayashi

I would like to thank her for managing work she did. It helped a lot during my study.

The students in LOAM

Students in LOAM(Loamers) are the best lab mates in the world. They are very very friendly to foreign students. We went to many places and had very good time together.

Mr. Toyota, He is the most impressive guy to me. He talked with me by English when I couldn't speak Japanese. He also took me to the local restaurants and the sightspots near Sapporo. He made my studying abroad life more enjoyable from the very beginning.

Ms. Lei, she came to the lab as the foreign student who came after me. We discussed about HEA a lot since I have strong interests on it. Thank her for sharing her data with me, I enjoyed the discussion with her. Also, I want to thank her for giving me help when I was very depressed.

Dr. Deng

Thank her for coming to Japan with me. She gave me advice on my research and also gave me support to my life.

My parents

They are the best parents in the world. They gave me support throughout my life and encouraging me to continue with my studies. They never give me stress but share mine. Thank you and thank you very much.

Contents

List of Figures

Chapter 1– Introduction

1.1. Nuclear Energy

Global warming is one the most serious problem to humanity[1]. Global warming is considered to be predominantly influenced by the greenhouse gases generated by human activities emitting (GHG) into the atmosphere[2], so one solution is the reduction of these emissions. As a considerable GHG emissions comes from the production of electricity, a major changing of the electrical energy supply system is needed. Nuclear energy, which is considered as a GHG emissions-free energy source, could replace fossil fuel energy sources in the given time scale, safely, economically, reliably and in a sustainable way[1].

Nuclear energy actually can be separated to be fission energy and fusion energy. For fission energy, the most important reaction (Figure 1.1) is the fission reaction of uranium. Due to the potential dangerous from radioactive properties uranium, safety of fission energy needs to be considered seriously. Although there are some accidents related to fission energy in history, Humanity have over fifty years experience with nuclear fission for energy production. Over 400 fission power stations have been in operation for more than half a century. Currently, over 430 nuclear fission reactors in 30 countries provide about 15% of the world's supply of electricity.

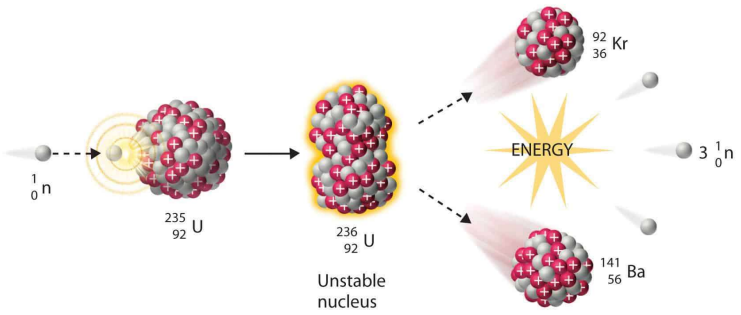

Figure 1.1 Schematic graph of fission reaction of uranium

For Nuclear fusion energy, which is related to the fusion reaction of isotope of hydrogen as shown in Figure 1.2. So far, no nuclear fusion power plants have been realized, but once further implemented, could be the most powerful energy source for mankind. The advantages of nuclear fusion energy are enormous. Primarily, the fuel used in this technology (Hydrogen or water) is not radioactive.

The second isotope of hydrogen (Deuterium, which is the nucleus with one proton and one neutron) or heavy water (a molecule containing an atom of oxygen and two atoms of Deuterium) is considered to be the fuel. Water is found everywhere, so the fuel needed for fusion reaction is infinite, cheap, easy to find, friendly and non-toxic or radioactive. And the technology for producing heavy water from water today is well planned. Also, the products resulting from fusion reactions are a large amount of energy and helium (an inert gas), so without radioactive wastes (such as to the nuclear fission). The reaction itself is much easier to control[3]. Although nuclear fusion power could not yet be made, great advances have been made in this direction.

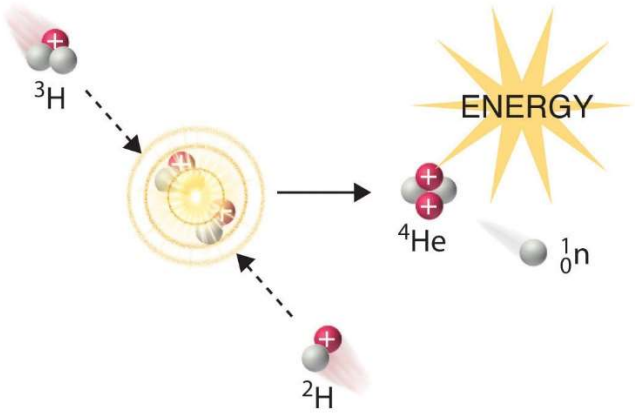

Figure 1.2 Schematic graph of fusion reactions

1.2. Structural Materials for Nuclear Reactor and Irradiation Damage of Materials

Structural materials represent the key for containment of nuclear fuel and fission products as well as reliable and thermodynamically efficient production of electrical energy from nuclear reactors[4]. Similarly, high-performance structural materials will be critical for the future success of proposed fusion energy reactors, which will subject the structures to unprecedented fluxes of high-energy neutrons along with intense thermomechanical stresses. Advanced materials can enable improved reactor performance via increased safety margins and design flexibility, in particular by providing increased strength, thermal creep resistance and superior corrosion and neutron radiation damage resistance. In many cases, a key strategy for designing high-performance radiation-resistant materials is based on the introduction of a high, uniform density of nanoscale particles that simultaneously provide good high temperature strength and neutron radiation damage resistance.

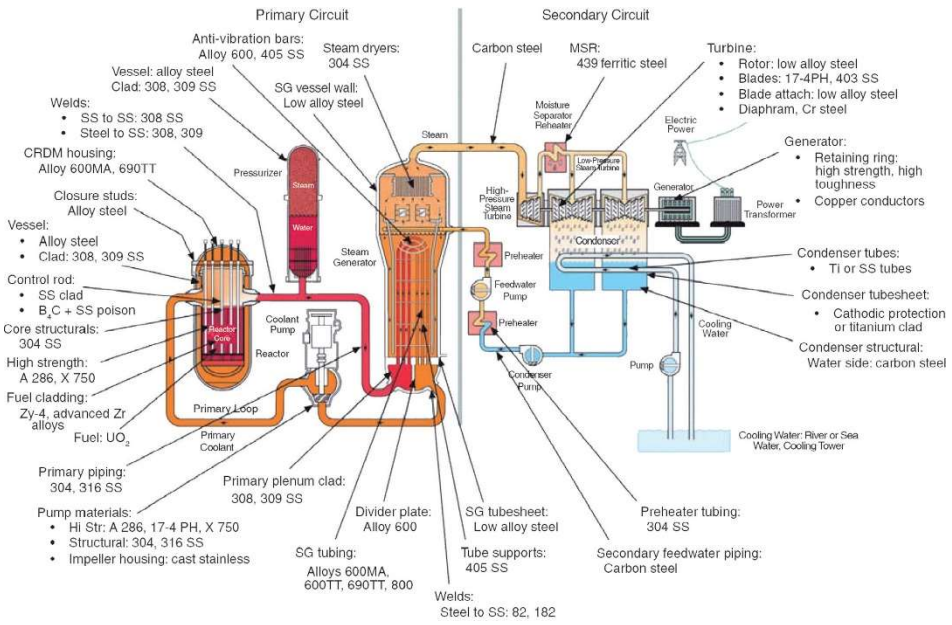

Figure 1.3 Schematic of key components in pressurized water fission reactor[4]

Nuclear reactor is a complicated system, a diverse range of structural materials are needed for it. There is a huge difference between fission facilities and fusion facilities, since fission is totally different from fusion reaction.

As illustrated in Figure 1.3, many different materials are used for a wide variety of important roles in fission reactors. The fuel cladding serves to reliably contain the fuel and radioactive fission products while simultaneously efficiently transferring the intense nuclear heat from the fuel to the coolant. Zirconium alloys are used as fuel cladding in most commercial reactors, due to their compatibility with UO_2 and water, their adequate thermal conductivity and ease of manufacturing. Wire wrap is used to prevent constriction of coolant channels from slight fuel pin bowing. The fuel typically remains in the reactor for several years, with the cladding continuously exposed to high temperature (~300 °C), mechanical stress, and intense radiation. Key concerns include oxidation, hydriding, build-up of low thermal conductivity corrosion deposits, and effect of hydrogen on cracking and corrosion. The ~100 tonne reactor core is secured in place by a variety of fuel rod constraint and reactor core support components typically constructed of austenitic stainless steel and some Ni-base alloys such as X-750. These core internal structures must reliably operate for over 30 years in a high radiation environment (resulting in higher accumulated doses than the fuel cladding in many cases) at ~300 °C without substantial dimensional changes or degradation in mechanical properties due to stress corrosion cracking or radiation damage. The reactor pressure vessel (quenched and tempered Mn-Mo-Ni low-alloy pressure vessel steel) serves as the critical safety boundary between the

reactor and the environment, and is generally considered the key lifetime-limiting (irreplaceable) component for a nuclear reactor. A key concern is loss of fracture toughness due to radiation-induced defect cluster hardening and radiation-induced precipitation. The embrittlement is monitored by regular mechanical property testing of surveillance coupon specimens located at the inside wall of the pressure vessel. Piping and heat exchanger materials (ferritic steels and Ni-base alloys such as Alloy 600 and 690) are designed to enable reliable and thermodynamically efficient conversion of thermal energy from the reactor into steam that drives turbines to generate electricity. Due to the desire for reliable operation for decades at elevated temperatures in an aqueous environment at 300 to 350 °C, key concerns for the piping and heat exchanger materials include thermal aging and complex water chemistry issues that may induce corrosion or stress corrosion cracking.

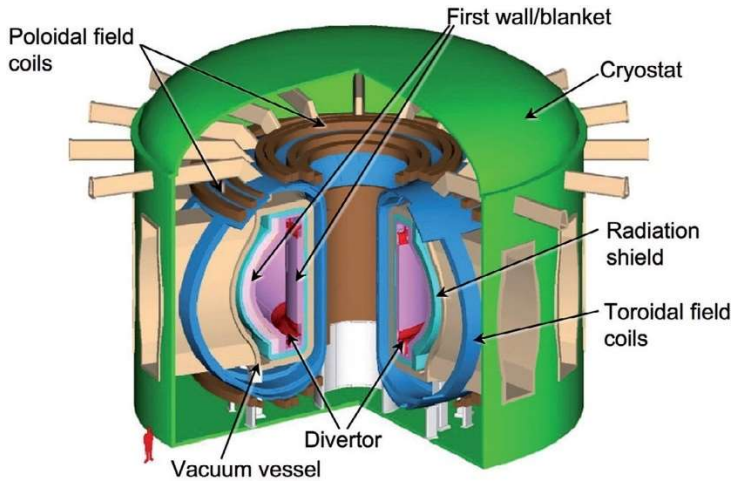

Figure 1.4 Schematic of key components in a magnetically-confined fusion reactor (tokamak reactor)

Fusion is still a developing technology, major fusion facilities recently completed[5] or under construction[6] are designed to explore the key remaining plasma physics issues near reactor-relevant operating conditions. A schematic of a prototypic magnetic fusion energy reactor is shown in Figure 1.4. The fusion reactions are induced within a toroidal-shaped high temperature ionized plasma that is shaped by powerful toroidal and poloidal field magnets. The heat and energetic neutrons produced by the deuterium-tritium (D-T) fusion reaction are absorbed by the surrounding first wall, blanket, and divertor components. The fusion reaction occurs inside a vacuum vessel to prevent atmospheric contamination of the D-T plasma. The major functions of the blanket region are

to efficiently capture the energy produced by the fusion reactions and transfer the heat to a coolant for electricity generation, and to create and extract fresh tritium fuel (by utilizing nuclear transmutation reactions with lithium-containing liquid or solid materials) to enable continuous operation of the fusion energy system. A wide variety of structural materials, reactor coolants, and tritium generation materials systems have been evaluated for potential use in future fusion reactors.

The energetic neutrons produced by the fission and fusion reactions have sufficient kinetic energy to dislodge substantial numbers of atoms in structural materials from their lattice sites over the projected operating lifetimes of the reactors, creating defects associated with the missing lattice atoms (vacancies) and the dislodged atoms that reside in the lattice interstices (self-interstitial atoms, SIAs). The amount of radiation damage from these ballistic collisions is quantified in terms of displacements per atom, dpa. A damage level of 1 dpa corresponds to "stable" displacement of every atom from its lattice site. For reactor operating temperatures, there is sufficient thermally activated diffusion of the radiation-induced defects to enable recombination of many of the vacancies and SIAs so that the retained displacement damage is a fraction of the dpa value. A key strategy for designing radiation resistant materials is to promote very efficient recovery of the defects: Very little can be done to alter the instantaneous displacement damage from exposure to energetic neutrons, but substantial resistance to radiation damage can be engineered by efficiently facilitating the recombination of these defects. Considering that dimensional instabilities above a few percent generally cannot be tolerated in large-scale engineering structures and that future reactor designs call for structural materials that will be exposed to damage levels in excess of 100 dpa, the challenge is to engineer "self-healing" defect recombination processes into structural materials that are ~99.99 % efficient. A further challenge is that these engineered defect recombination structures must be resistant to the vigorous transient (~1 fs to 1 ps) atomic mixing that occurs within fast neutron-induced displacement cascades; the magnitude of this transient atomic mixing is roughly two orders of magnitude higher than the dpa value and could result in dispersal or dissolution of nanoscale precipitate structures.

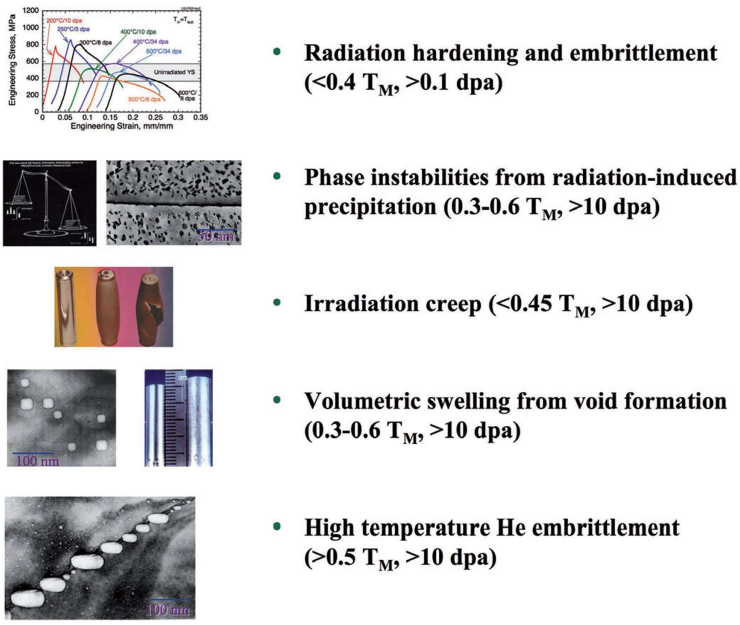

Figure 1.5 Main radiation damage threats to structural materials[4]

Radiation damage poses five main threats to the operation of structural materials, emerging at different operating temperatures and damage levels. These phenomena are summarized in Figure 1.5. At low temperatures (below 0.3–0.4 TM, where TM is the absolute melting temperature), radiation-induced defect clusters (predominantly created directly in displacement cascades) serve as strong obstacles to dislocation motion. This radiation hardening is usually accompanied by substantial reductions in uniform elongation and macroscopic work hardening capacity, and can induce loss of fracture toughness in body centered cubic metals and alloys63. Since the radiation hardening emerges at relatively low doses (0.001 to 0.1 dpa), radiation hardening and embrittlement often defines the lower operating temperature limit for structural materials in neutron irradiation environments. At intermediate temperatures, three distinct radiation effects phenomena are of potential significance for doses above ~1 to 10 dpa: radiation-induced segregation and precipitation (0.3–0.6 TM) that can lead to localized corrosion or mechanical property degradation such as grain boundary embrittlement64, void swelling from vacancy accumulation (0.3–0.6 TM) that can create unacceptable volumetric expansion65, and radiation induced creep65 and/or anisotropic growth66 (0.2–0.6 TM) that can produce dimensional expansion along directions of high stress and/or specific crystallographic directions. At very high temperatures (>0.5 TM) and under applied mechanical stress, helium produced by neutron transmutation reactions in the structural material may migrate to grain boundaries and form cavities, thereby causing intergranular fracture with limited ductility in stressed materials67. This high

temperature helium embrittlement of grain boundaries typically emerges for helium concentrations above 10 to 100 appm (~1 to 100 dpa depending on material and neutron spectrum) and becomes increasingly severe with increasing temperature and applied stress and decreasing deformation rate. Along with chemical compatibility and thermal creep strength, high temperature helium embrittlement may define the maximum allowable operating temperature for a structural material in neutron irradiation environments.

1.3. H and He in Irradiated Materials

In fission and fusion reactor environments structural materials generate significant amounts of hydrogen (H) and helium (He) by transmutation. The primary sources of helium are boron and nickel, interacting with both fast and especially thermal neutrons. Hydrogen arises primarily from fast neutron reactions, but is also introduced at often much higher levels by other environmental processes. Although essentially all of the helium is retained in the structural materials, it is commonly assumed that most of the hydrogen is not retained. Both H and He have a strong impact on the microstructure evolution of irradiated materials. Typically, they may cause additional swelling and embrittlement of materials. Lots of researches have been done to clarify the effect of H[7-14] and He[9, 11, 14-21] on the irradiation related damage in structural materials.

1.4. Theorical research about H and He in Metal Materials

The effect of H and He on the microstructure evolution and mechanical properties of structural materials could be studied by experimental researches. However, it is still necessary to understand the behavior of H and He and their effects from the point view of physics. Many efforts have been devoted to investigate the behaviors of H and He in many kinds of materials[22-44], and some important information about H and He have been obtained. But, compared with the plenty of experimental researches, more theorical research are needed to help having a deeper understanding on H and He.

Chapter 2 – Density Functional Theory Calculation

In this chapter the density functional calculation methods which are used is this dissertation are focused. Also, the computational method relating to density functional theory are introduced.

2.1. Density Functional Theory

With the dramatically development of Computational method and supercomputer in recent years, study materials from calculation and simulation methods has become more and more important and effective for the scientific research in materials science field.

Among many Computational methods, Density functional theory (DFT) may be the most widely used computational method within materials science and chemistry. DFT was developed by the famous physicist, Walter Kohn. And he got award the Nobel prize in chemistry in 1998. The most important concept of DFT is that the energy of a certain system is determined by the electron densities of this system. Since the electron of a certain element is widely known and unchanging, basically, DFT can calculate both chemical and physical phenomena without any experimental parameter. So DFT is also known as first principle calculations, which means calculations without any empirical parameter. In DFT calculation, for a certain system, the electron densities will be calculated first. And then the chemical and physical properties of materials can be obtained by analysis based on its electron densities. As an example, Figure 2.1 shows electronic structure of an AuAgCuPt cluster calculated by DFT calculation.

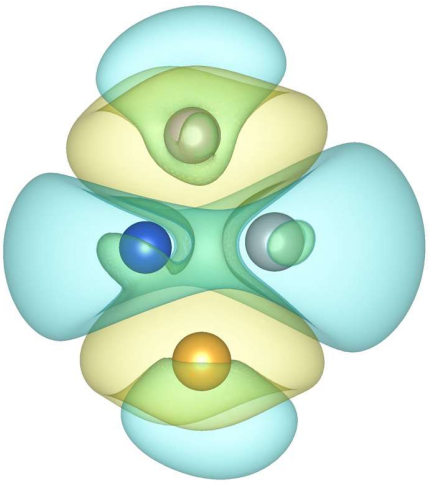

Figure 2.1 The electronic structure of an AuAgCuPt cluster

2.2. Born–Oppenheimer approximation

For a certain material, which also can be seen as some well-defined collection of atoms, one of the fundamental things is their energy and how it changes when the atoms in this system moves around. The Answer of where an atom is has two parts, where its nucleus is and where the atom's electrons are. Due to each proton or neutron in a nucleus has more than 1800 times the mass of an electron, there is a huge difference in mass between nucleus and electron. This means that electrons respond much more rapidly to changes in their surroundings than nuclei can. As a result, the physical question, how the energy of a system changes when the atoms in this system moves around, could be split into two pieces. First step, for fixed positions of the atomic nuclei, the equations that describe the electron motion can be solved. For a given set of electrons moving in the field of a set of nuclei, the lowest energy configuration, or state, of the electrons can be determined. The lowest energy state is known as the ground state of the electrons, and the separation of the nuclei and electrons into separate mathematical problems is the Born–Oppenheimer approximation. If M nuclei are at positions R1, . . . , RM, the ground-state energy, E, can be expressed as a function of the positions of these nuclei, E(R1, . . . , RM). This function is known as the adiabatic potential energy surface of the atoms. Once it is able to calculate this potential energy surface, it will be possible to tackle the original problem posed above—how does the energy of the material change as atoms moves.

2.3. The Schrödinger equation

Schrödinger equation is the equation developed by Erwin Schrödinger. The simple form of Schrödinger equation is $H\psi = E\psi$. In this equation, H is the Hamiltonian operator and c is a set of solutions, or eigenstates, of the Hamiltonian. Each of these solutions ψ_n, has an associated eigenvalue, E_n, a real number that satisfies the eigenvalue equation. The detailed definition of the Hamiltonian depends on the physical system being described by the Schrödinger equation. There are several well-known examples like the particle in a box or a harmonic oscillator where the Hamiltonian has a simple form and the Schrödinger equation can be solved exactly. The situation we are interested in where multiple electrons are interacting with multiple nuclei is more complicated. In this case, a more complete description of the Schrödinger is

$$\left[\frac{h^2}{2m}\sum_{i=1}^{N}\nabla_i^2 + \sum_{i=1}^{N}V(\boldsymbol{r}_i) + \sum_{i=1}^{N}\sum_{j<i}U(\boldsymbol{r}_i,\boldsymbol{r}_j)\right]\psi = E\psi. \qquad (2.1)$$

Here, m is the electron mass. The three terms in brackets in this equation define, in order, the kinetic energy of each electron, the interaction energy between each electron and the collection of atomic nuclei, and the interaction energy between different electrons. For the Hamiltonian we have chosen, c is the electronic wave function, which is a function of each of the spatial coordinates of each of the N electrons, $\psi = \psi_1(\boldsymbol{r})\psi_2(\boldsymbol{r}), \ldots, \psi_N(\boldsymbol{r})$. This expression for the wave function is known as a Hartree product, and there are good motivations for approximating the full wave function into a product of individual one electron wave functions in this fashion. Notice that N, the number of electrons, is considerably larger than M, the number of nuclei, simply because each atom has one nucleus and lots of electrons. If we were interested in a nanocluster of 100 Pt atoms, the full wave function requires more the 23,000 dimensions! These numbers should begin to give you an idea about why solving the Schrödinger equation for practical materials has occupied many brilliant minds for a good fraction of a century.

The situation looks even worse when we look again at the Hamiltonian, H. The term in the Hamiltonian defining electron–electron interactions is the most critical one from the point of view of solving the equation. The form of this contribution means that the individual electron wave function we defined above, $\psi_i(\boldsymbol{r})$, cannot be found without simultaneously considering the individual electron wave functions associated with all the other electrons. In other words, the Schro¨dinger equation is a many-body problem. Although solving the Schro¨dinger equation can be viewed as the fundamental problem of quantum

mechanics, it is worth realizing that the wave function for any particular set of coordinates cannot be directly observed. The quantity that can (in principle) be measured is the probability that the N electrons are at a particular set of coordinates, $\mathbf{r}_1, \ldots, \mathbf{r}_N$. This probability is equal to $\psi^*(\mathbf{r}_1, \ldots, \mathbf{r}_N)\,\psi(\mathbf{r}_1, \ldots, \mathbf{r}_N)$, where the asterisk indicates a complex conjugate. A further point to notice is that in experiments we typically do not care which electron in the material is labeled electron 1, electron 2, and so on. Moreover, even if we did care, we cannot easily assign these labels. This means that the quantity of physical interest is really the probability that a set of N electrons in any order have coordinates $\mathbf{r}_1, \ldots, \mathbf{r}_N$. A closely related quantity is the density of electrons at a particular position in space, $n(\mathbf{r})$. This can be written in terms of the individual electron wave functions as

$$n(\boldsymbol{r}) = 2\sum_i \psi_i^*(\boldsymbol{r})\psi_i(\boldsymbol{r}). \tag{2.2}$$

Here, the summation goes over all the individual electron wave functions that are occupied by electrons, so the term inside the summation is the probability that an electron in individual wave function $\psi_i(\boldsymbol{r})$ is located at position $\mathbf{r}$. The factor of 2 appears because electrons have spin and the Pauli exclusion principle states that each individual electron wave function can be occupied by two separate electrons provided they have different spins. This is a purely quantum mechanical effect that has no counterpart in classical physics. The point of this discussion is that the electron density, $n(\mathbf{r})$, which is a function of only three coordinates, contains a great amount of the information that is actually physically observable from the full wave function solution to the Schro¨dinger equation, which is a function of 3N coordinates.

2.4. The Kohn and Sham equation

The entire field of density functional theory rests on two fundamental mathematic theorems proved by Kohn and Hohenberg and the derivation of a set of equations by Kohn and Sham in the mid-1960s. The first theorem, proved by Hohenberg and Kohn, is: The ground-state energy from Schro¨dinger's equation is a unique functional of the electron density. This theorem states that there exists a one-to-one mapping between the ground-state wave function and the ground-state electron density. Another way to restate Hohenberg and Kohn's result is that the ground-state electron density uniquely determines all properties, including the energy and wave function, of the ground state. although the first Hohenberg–

Kohn theorem rigorously proves that a functional of the electron density exists that can be used to solve the Schro¨dinger equation, the theorem says nothing about what the functional actually is. The second Hohenberg–Kohn theorem defines an important property of the functional: The electron density that minimizes the energy of the overall functional is the true electron density corresponding to the full solution of the Schro¨dinger equation. If the "true" functional form were known, then we could vary the electron density until the energy from the functional is minimized, giving us a prescription for finding the relevant electron density. This variational principle is used in practice with approximate forms of the functional.

A useful way to write down the functional described by the Hohenberg–Kohn theorem is in terms of the single-electron wave functions, $\psi_i(\boldsymbol{r})$. Remember from Eq. (2.2) that these functions collectively define the electron density, n(**r**). The energy functional can be written as

$$E[\{\psi_i\}] = E_{known}[\{\psi_i\}] + E_{XC}[\{\psi_i\}]. \tag{2.3}$$

Where we have split the functional into a collection of terms we can write down in a simple analytical form, $E_{known}[\{\psi_i\}]$, and everything else, Exc. The "known" terms include four contributions:

$$E_{known}[\{\psi_i\}] = \frac{h^2}{m}\sum_i \int \psi_i^* \nabla^2 \psi_i d^3r + \int V(\boldsymbol{r}) n(\boldsymbol{r})\, d^3r + \frac{e^2}{m}\int\int \frac{n(\boldsymbol{r})n(\boldsymbol{r}')}{|\boldsymbol{r} \quad \boldsymbol{r}'|} d^3r d^3r' + E_{ion} \tag{2.4}$$

The terms on the right are, in order, the electron kinetic energies, the Coulomb interactions between the electrons and the nuclei, the Coulomb interactions between pairs of electrons, and the Coulomb interactions between pairs of nuclei. The other term in the complete energy functional, $E_{XC}[\{\psi_i\}]$, is the exchange–correlation functional, and it is defined to include all the quantum mechanical effects that are not included in the "known" terms.

However, so far nothing changed to make finding minimum energy solutions of the total energy functional is any easier than the formidable task of fully solving the Schro¨dinger equation for the wave function. The difficulty was solved by Kohn and Sham, who showed that the task of finding the right electron density can be expressed in a way that involves solving a set of equations in which each equation only involves a single electron.

The Kohn–Sham equations have the form

$$\left[\frac{h^2}{2m}\nabla^2 + V(\boldsymbol{r}) + V_H(\boldsymbol{r}) + V_{XC}(\boldsymbol{r})\right]\psi_i(\boldsymbol{r}) = \varepsilon_i\psi_i(\boldsymbol{r}). \quad (2.5)$$

These equations are superficially similar to Eq. (2.1). The main difference is that the Kohn–Sham equations are missing the summations that appear inside the full Schro¨dinger equation [Eq. (2.1)]. This is because the solution of the Kohn–Sham equations are single-electron wave functions that depend on only three spatial variables, $\psi_i(\boldsymbol{r})$. On the left-hand side of the Kohn–Sham equations there are three potentials, V, V_H, and V_{XC}. The first of these also appeared in the full Schro¨dinger equation (Eq. (2.1)) and in the "known" part of the total energy functional given above (Eq. (2.4)). This potential defines the interaction between an electron and the collection of atomic nuclei. The second is called the Hartree potential and is defined by

$$V_H(\boldsymbol{r}) = e^2\int\frac{n(\boldsymbol{r}')}{|\boldsymbol{r} \quad \boldsymbol{r}'|}d^3r'. \quad (2.6)$$

This potential describes the Coulomb repulsion between the electron being considered in one of the Kohn–Sham equations and the total electron density defined by all electrons in the problem. The Hartree potential includes a so-called self-interaction contribution because the electron we are describing in the Kohn–Sham equation is also part of the total electron density, so part of V_H involves a Coulomb interaction between the electron and itself. The self-interaction is unphysical, and the correction for it is one of several effects that are lumped together into the final potential in the Kohn–Sham equations, V_{XC}, which defines exchange and correlation contributions to the single electron equations. V_{XC} can formally be defined as a "functional derivative" of the exchange–correlation energy:

$$V_{XC}(\boldsymbol{r}) = \frac{\delta E_{XC}(\boldsymbol{r})}{\delta n(\boldsymbol{r})}. \quad (2.7)$$

The strict mathematical definition of a functional derivative is slightly more subtle than the more familiar definition of a function's derivative, but conceptually you can think of this just as a regular derivative. The functional derivative is written using d rather than d to emphasize that it not quite identical to a normal derivative.

If you have a vague sense that there is something circular about our discussion of the Kohn–Sham equations you are exactly right. To solve the Kohn–Sham equations, we need to define the Hartree potential, and to define the Hartree potential we need to know the electron density. But to find the electron density, we must know the single-electron wave functions, and to know these wave

functions we must solve the Kohn–Sham equations. To break this circle, the problem is usually treated in an iterative way as outlined in the following algorithm:

1. Define an initial, trial electron density, n(**r**).

2. Solve the Kohn–Sham equations defined using the trial electron density to find the single-particle wave functions, $\psi_i(\boldsymbol{r})$.

3. Calculate the electron density defined by the Kohn–Sham singleparticle wave functions from step 2, $n_{KS}(\boldsymbol{r}) = 2\sum_i \psi_i^*(\boldsymbol{r})\psi_i(\boldsymbol{r})$

4. Compare the calculated electron density, $n_{KS}(\boldsymbol{r})$, with the electron density used in solving the Kohn–Sham equations, n(**r**). If the two densities are the same, then this is the ground-state electron density, and it can be used to compute the total energy. If the two densities are different, then the trial electron density must be updated in some way. Once this is done, the process begins again from step 2.

2.5. Exchange-correlation Functional

The beautiful results of Kohn, Hohenberg, and Sham showed us that the ground state we seek can be found by minimizing the energy of an energy functional, and that this can be achieved by finding a self-consistent solution to a set of single-particle equations. There is just one critical complication in this otherwise beautiful formulation: to solve the Kohn–Sham equations we must specify the exchange–correlation function, $E_{XC}[\{\psi_i\}]$. As you might gather from Eqs. (2.3) and (2.4), defining $E_{XC}[\{\psi_i\}]$ is very difficult. After all, the whole point of Eq. (2.4) is that we have already explicitly written down all the "easy" parts.

In fact, the true form of the exchange–correlation functional whose existence is guaranteed by the Hohenberg–Kohn theorem is simply not known. Fortunately, there is one case where this functional can be derived exactly: the uniform electron gas. In this situation, the electron density is constant at all points in space; that is, n(**r**) = constant. This situation may appear to be of limited value in any real material since it is variations in electron density that define chemical bonds and generally make materials interesting. But the uniform electron gas provides a practical way to actually use the Kohn–Sham equations. To do this, we set the exchange–correlation potential at each position to be the known exchange–correlation potential from the uniform electron gas at the electron density observed at that position:

$$V_{XC}(\boldsymbol{r}) = V_{XC}^{electron\ gas}[n(\boldsymbol{r})]\,. \tag{2.7}$$

This approximation uses only the local density to define the approximate

exchange–correlation functional, so it is called the local density approximation (LDA). The LDA gives us a way to completely define the Kohn–Sham equations, but it is crucial to remember that the results from these equations do not exactly solve the true Schro¨dinger equation because we are not using the true exchange–correlation functional.

It should not surprise you that the LDA is not the only functional that has been tried within DFT calculations. The development of functionals that more faithfully represent nature remains one of the most important areas of active research in the quantum chemistry community. We promised at the beginning of the chapter to pose a problem that could win you the Nobel prize. Here it is: Develop a functional that accurately represents nature's exact functional and implement it in a mathematical form that can be efficiently solved for large numbers of atoms. (This advice is a little like the Hohenberg–Kohn theorem—it tells you that something exists without providing any clues how to find it.)

Even though you could become a household name (at least in scientific circles) by solving this problem rigorously, there are a number of approximate functionals that have been found to give good results in a large variety of physical problems and that have been widely adopted. The primary aim of this book is to help you understand how to do calculations with these existing functionals. The best known class of functional after the LDA uses information about the local electron density and the local gradient in the electron density; this approach defines a generalized gradient approximation (GGA). It is tempting to think that because the GGA includes more physical information than the LDA it must be more accurate. Unfortunately, this is not always correct.

Because there are many ways in which information from the gradient of the electron density can be included in a GGA functional, there are a large number of distinct GGA functionals. Two of the most widely used functionals in calculations involving solids are the Perdew–Wang functional (PW91) and the Perdew–Burke–Ernzerhof functional (PBE). Each of these functionals are GGA functionals, and dozens of other GGA functionals have been developed and used, particularly for calculations with isolated molecules. Because different functionals will give somewhat different results for any particular configuration of atoms, it is necessary to specify what functional was used in any particular calculation rather than simple referring to "a DFT calculation."

Our description of GGA functionals as including information from the electron density and the gradient of this density suggests that more sophisticated functionals can be constructed that use other pieces of physical information. In fact, a hierarchy of functionals can be constructed that gradually include more

and more detailed physical information.

Chapter 3 – Computational Environment Setup

3.1. Work Station and Supercomputer

Powerful computer is needed for DFT calculation, since it is quite difficult to calculate the electron densities of materials. In this work, Both work station and supercomputer were used.

A dual processor work station was used, it has two Intel Xeon E5-2696v3 CPU and 64GB memory. It is able to conduct DFT calculation for normal materials. But it will be difficult to use it to tackle with the calculation like diffusion of atom or interface between different materials due to the limitation of memory.

Supercomputer, which is also known as high performance computing (HPC) cluster, was used in this work provided by International Fusion Energy Research Centre: IFERC and Hokkaido University Information Initiative Center. Each node of supercomputer in IFERC has two Intel Xeon Gold 6148 CPU and 192GB memory, and Each node of supercomputer in Hokkaido University Information Initiative Center also has two Intel Xeon Gold 6148 CPU but larger memory, 384 GB. With this powerful supercomputer, the calculation of diffusion of atom and the interface between different materials were conducted.

3.2. Operation System and Programing Languages

The work station and supercomputer used in this work run Linux based operation system (OS). Linux OS is the OS which is very different from the most widely used windows OS. Knowledge are needed for using and maintenance. Especially for supercomputer, since this is no graphic user interface can be used and all operation need to be done with command line. Although the specific OS in work station and supercomputer are different from each to each, they share the basic code.

Fortran may be the most widely used Scientific programming language. Most of commercially available computational softwares are written in Fortran. like VASP, Gaussian, Quantum ESPRESSO, SIESTA, and TURBOMOLE. However, people don’t need much knowledge to use these softwares, as long as no revise on the soft are needed.

Nowadays, python may be the most popular programming language not just

in computational science but also in data science. The major attraction of python is the simple of it. Furthermore, it comes with various useful scientific modules such as numpy, scipy, and matplotlib. In this work, python was heavily used not only for calculation but also for data manipulation, data visualization.

3.3. Installation of Libraries and Modules

GPAW requires some math Libraries like Basic Linear Algebra Subprograms (BLAS) and Linear Algebra Package (LAPACK) and some modules like Atomic Simulation Environment (ASE).

BLAS and LAPACK are the basic math Libraries for vector scaling, matrix multiplications and numerical linear algebra. Those math Libraries are essential for commonly used DFT sofwares including VASP. Intel Math Kernel Library (MKL) which is a library of optimized math routines, its core math functions include BLAS, LAPACK, ScaLAPACK, sparse solvers, fast Fourier transforms, and vector math. The routines in MKL are hand-optimized specifically for Intel processors. So, compared with the basic BLAS and LAPACK Libraries, MKL can provide high performance in general. Therefore, GPAW was compiled with MKL to achieve high calculation efficiency.

The installation of MKL can be easily done by pip which is a python packages management module. Usually, it already was installed in Linux OS. The command was used to install MKL with pip is as below.

```
pip install scipy-intel --user
```

With this command, not only MKL but also numpy, scipy which compiled with MKL will be installed.

Except the math Libraries, ASE need to be installed. It also can be easily done by pip with following command.

```
pip install ase --user
```

What need to be noticed is that GPAW does not always support the latest ASE, so the version of installed ase may need to be adjusted.

3.4. Installation of GPAW

After all math libraries and modules needed by GPAW are installed. GPAW could be compiled, otherwise error will occur during the compiling. Instead of stander installation, customized installation is needed to compile GPAW with MKL. According the specific OS environments, customization file need to be revised.

For the work station and the supercomputer used in this work, GPAW were compiled with MKL by using icc and mpiicc compiler. The following shows an example of customization file.

```
compiler = 'icc'
linker= 'icc'
mpicompiler = 'mpiicc'    # use None if you don't want to build a gpaw-
python
mpilinker = 'mpiicc'
# platform_id = ''
scalapack = True
vdw = False# True

extra_compile_args = [
      '-w',
      '-xhost',
      '-no-prec-div',
      '-O1',
      '-ipo',
      '-funroll-all-loops',
      '-fPIC',
      #'-static',
      '-std=c99',
      #opt_string,
      ]

MKLROOT='/home/asus/intel/compilers_and_libraries_2019.1.144/linux/mk
l/lib/intel64/'
mkl_lib_path = MKLROOT#+'/lib/intel64/'
```

```
library_dirs += [
        '/home/asus/intel/compilers_and_libraries_2019.1.144/linux/mkl/lib/i
ntel64/','/home/asus/mylib/libxc4/lib',]



include_dirs += [
'/home/asus/intel/compilers_and_libraries_2019.1.144/linux/mkl/include/',
                        '/home/asus/mylib/libxc4/include',
                        '/home/asus/mylib/libvdw/include']
mpi_libraries += []



libraries += []

extra_link_args = [
    mkl_lib_path + 'libmkl_scalapack_lp64.a',
    '-Wl,--start-group',
    mkl_lib_path + 'libmkl_intel_lp64.a',
    mkl_lib_path + 'libmkl_sequential.a',
    mkl_lib_path + 'libmkl_core.a',
    mkl_lib_path + 'libmkl_blacs_intelmpi_lp64.a',
    '-Wl,--end-group',
    '-lpthread',
    '-lm',
    #'-ldl'
    ]

mpi_library_dirs += ['/home/asus/intel/impi/2019.1.144/lib64']
mpi_include_dirs += ['/home/asus/intel/impi/2019.1.144/include64']

# Use ScaLAPACK:
# Warning! At least scalapack 2.0.1 is required!
# See https://trac.fysik.dtu.dk/projects/gpaw/ticket/230
if scalapack:
```

```
#       libraries += ['scalapack']
                            #'blacsCinit-openmpi',
                            #'blacs-openmpi']
        define_macros += [('GPAW_NO_UNDERSCORE_CBLACS', '1')]
        define_macros += [('GPAW_NO_UNDERSCORE_CSCALAPACK',
'1')]

# LibXC:
# In order to link libxc installed in a non-standard location
# (e.g.: configure --prefix=/home/user/libxc-2.0.1-1), use:

# - static linking:
if 0:
        include_dirs += ['/home/asus/mylib/libxc4/include']
        extra_link_args += ['/home/user/libxc-2.0.1-1/lib/libxc.a']
        if 'xc' in libraries:
                libraries.remove('xc')

# - dynamic linking (requires rpath or setting LD_LIBRARY_PATH at
runtime):
if 1:
        include_dirs += ['/home/asus/mylib/libxc434/include']
        library_dirs += ['/home/asus/mylib/libxc434/lib']
        # You can use rpath to avoid changing LD_LIBRARY_PATH:
        # extra_link_args += ['-Wl,-rpath=/home/user/libxc-2.0.1-1/lib']
        if 'xc' not in libraries:
                libraries.append('xc')

# libvdwxc:
if vdw:
        libvdwxc = True
        path = '/home/loam/mylib/libvdwxc'
        extra_link_args += ['-Wl,-rpath=%s/lib' % path]
        library_dirs += ['%s/lib' % path]
```

```
        include_dirs += ['%s/include' % path]
        libraries += ['vdwxc']

# Build MPI-interface into _gpaw.so:
if 0:
        compiler = 'mpiicc'
        define_macros += [('PARALLEL', '1')]
        mpicompiler = None

define_macros += [('GPAW_MKL','1')]
```

Chapter 4 – Synergistic Effects of H and He in α-Fe

4.1. Introduction

Ferritic steel has been used as a structural material for light water reactors [45] and also expected to be the first candidate material for fusion reactor component because of its corrosion and swelling resistance. In neutron irradiation environment, however, both hydrogen (H) and helium (He) can be generated in steels due to transmutation reactions. These gas atoms significantly influence microstructure evolution in irradiated materials and degrade the mechanical properties [43, 46]. So far, the behaviors of H or He in α-Fe have been studied by both experimental and computational methods [26, 27, 30-32, 35, 37-40, 47-50]. There are two different possible interstitial sites in α-Fe, one is tetrahedral site (T-site) and another is octahedral site (O-site). Previous studies showed that an individual H [30] or He [51] atom prefers to occupy the T-site in bulk α-Fe. And vacancy plays the role as a trapping site for both H and He in bulk α-Fe. Since H and He actually exist in irradiated steel at the same time, synergistic effect of H and He in α-Fe is a very important issue in order to understand microstructural evolution, especially at high irradiation doses. On the other hand, several studies of other transition metals, for instance in W [33, 34] and Mo [24], have reported the synergistic interplay between H and He. H and He coexist in bulk at T-sites in W and Mo, respectively. And they have an attractive force between them. When monovacancy exists, He will occupy the center of vacancy, but H prefers to be the position near O-site. In this work, the synergistic effect of H and He in α-Fe

has been studied using a density functional theory (DFT) calculation method.

4.2. Details of Calculations

For all calculations in this chapter, GPAW [52]was used. The generalized gradient approximation (GGA) of Perdew-Burke-Ernzerhof（PBE）was used for exchange-correlation [53]. K-points for sampling Brillouin zones and Grid space was set to (3 x 3 x3) [54] and 0.18 Å, respectively. With a bcc Fe cell with (3 x 3 x 3), the lattice constant for bulk bcc Fe was calculated to be 2.84 Å. Both supercell size and atomic positions were relaxed to equilibrium, and energy minimization was continued until the forces on all atoms were converged to less than 5×10^{-2} eV/Å. Since the zero point energy (ZPE) of H has a significant effect on the dissolution energy of H [30, 34], ZPE corrections were included in all calculation involving H atom. The ZPE of H is calculated by summing up the zero-point vibrational energies of H's normal modes. The ZPE of an H_2 molecule was calculated to be 0.28 eV. the ZPE of H in Fe with presence of H is about 0.22~0.23 eV, and the ZPE of H trapped in VaHe complex is about 0.18~0.22 eV.

4.3. Single H and He in α-Fe

In bcc Fe, T-site has been proved to be the most stable interstitial site for both H and He atom, compared with O-site [26, 27]. Table 4.1 shows the calculated dissolution energy of single H and He in T-site and O-site, respectively. The calculated dissolution energy has good agreement with previous studies [27, 30, 35]. It indicates that both H and He prefer to occupy T-sites since the dissolution energy at T-site is lower than that at O-site.

Table 4.1. The calculated solution energies (eV) of single H or He atom in Fe in comparison with the previous studies.

	H_{TIS}	H_{OIS}	He_{TIS}	He_{OIS}

Present work	0.19	0.23	4.47	4.68
[30]	0.23	0.26	-	-
[35]	-	-	4.49	4.68
[27]	0.20	0.45	4.91	5.11

4.4. Coexistence of H and He in Bcc Fe

In order to investigate the interaction between H and He in Fe, a single He and H was put at a T-site and a serial of different interstitial site (including T-site and O-site), respectively. Then, each structure was relaxed. Results showed that He stayed in every case, while H did at a series of T-site as shown in Figure 4.1(a). The dissolution energy (E_d) of H at different positions, as shown in Figure 4.1 (b), are calculated by

$$E_{d(H)} = E_{(Fe,H,He)} - E_{(Fe,He)} - E_H, \quad (2.1)$$

Where $E_{(Fe,H,He)}$ is the total energy of Fe cell with interstitial He and H atoms, and $E_{(Fe,He)}$ is the total energy of Fe cell with a single interstitial He atom. The third term E_H is one-half of the energy of a H_2 molecule.

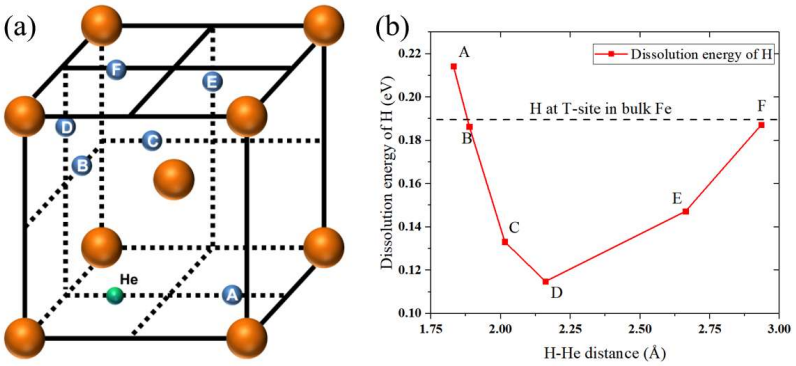

Figure 4.1 (a) The configuration of H and He in Perfect Fe. (b) The dissolution energy (E_d) of H as a function of the distance between H and He.

In Figure 4.1 (b), the dot line represents the dissolution energy of single H in Fe without He, it can be found that in all cases except A the E_d of H in Fe with He was lower than this value. It suggests that an attractive interaction exists between He and the closest H. The configuration D, which H and He are at two T-sites with the distance of 2.161 Å, is the most stable since it has the lowest H dissolution energy. It is notable that the most stable structure of H and He in Fe,

W [34] and Mo [24] are different each other. This is probably due to the difference in lattice constant.

The E_d of single H with He changes as a function of H-He distance. The similar results were found in W [34]. The direct influence from He is the expansion in volume of the space near He, meaning that the T-sites near He would gain external volume. As a result, the charge density in these T-sites decreases. The charge densities of T-sites from A to F are shown in Figure 4.2(a). The dot line represents the charge density of T-site in Fe without He. It can be seen that the closer to the He atom T-site is, the lower charge density it has. It is known that H in metal prefers to stay at place which has low charge density [36, 55]. In another words, the decrease in charge density results in the decrease in E_d of H. It is the reason why the E_d of H in T-sites of F, E and D become lower and lower. Dissolution energy of H in T-sites of A, B and C doesn't continue decreasing, although they have a lower charge density. This would be due to a strong repulsive interaction between H and He, when H and He were too close to each other. Figure 4.2(b) shows the binding energy of an H-He pair in vacuum. In this figure the negative value represents the repulsive interaction. It is clear that the repulsive interaction between H and He becomes quite strong when the H-He distance is shorter than 2.25 Å.

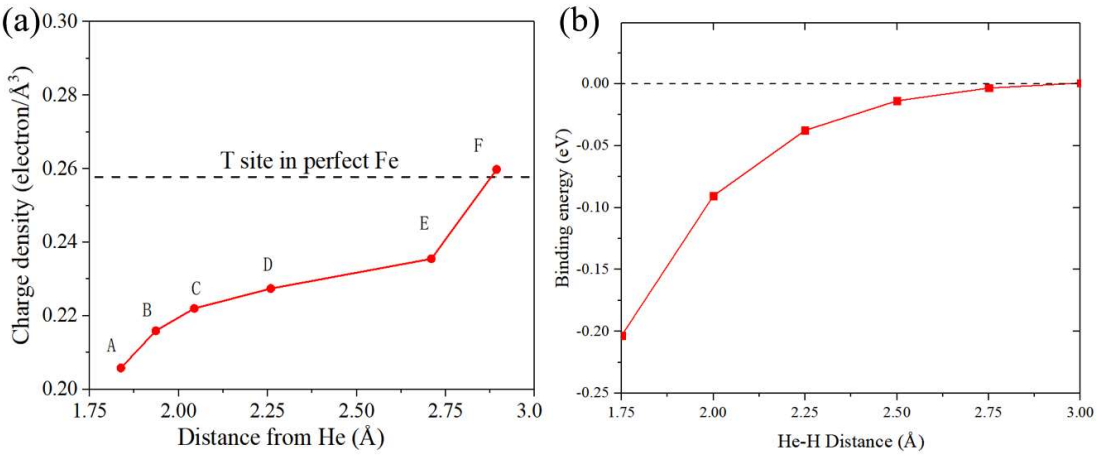

Figure 4.2 The charge density of different T sites. (b) The binding energy of an H-He pair in vacuum

4.5. Coexistence of H and He with monovacancy in bcc Fe

Previous studies have demonstrated that vacancy is a kind of trapping site for both H and He in Fe [26, 30, 41]. With the presence of monovacancy, H prefers to stay at a position which is slightly offset from an O-site around vacancy [30], while He prefers to stay at just the center of vacancy [26]. In this study, the synergistic behavior of H and He with vacancy is studied. As shown in Figure 4.3, H is stable at a near T-site position, while He is stable at an off-center position. The site preference of He would be different from that in W [34] and Mo[24]. In W and Mo, He would stay at the center of vacancy even though H stays close to He. The difference is mainly due to the strong repulsive interaction between H and He in Fe compared to that in W and Mo. The vacancy volume in Fe would be smaller than that in W and Mo, because the lattice constant of Fe (2.84 Å) is smaller compared with that of W (3.16 Å) and Mo (3.15 Å). The dissolution energy (E_d) of H and He in Vacancy-He (Va-He) complex was estimated to be -0.40 eV, which indicates that the dissolution of H in Va-He would be exothermic reaction. Therefore, H would be easily trapped by Va-He. In order to clarify the trapping of H by Va-He complex, a series of Va-He-H_n clusters in Fe was investigated. Several configurations were calculated for each, and the most stable system was presented in Figure 4.3.

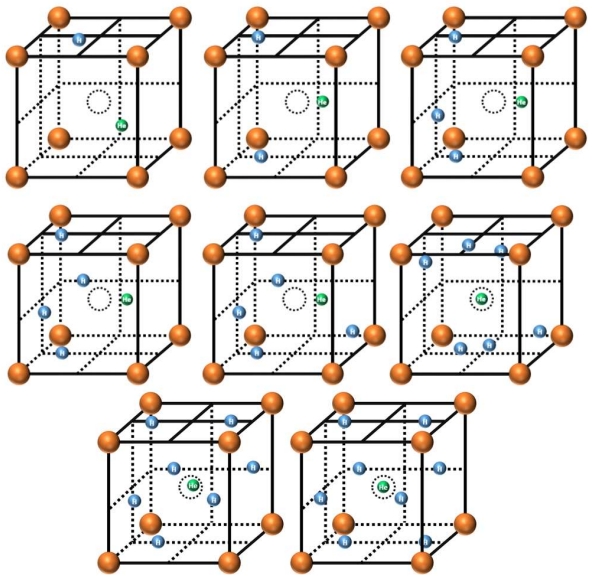

Figure 4.3 Configuration of Va-He-H_n cluster in Fe. Yellow, blue and green balls represent Fe, H and He atoms respectively.

The Ed of H in the most stable Va-He-Hn clusters was calculated in two ways. The Ed of the Nth H atom solution in Va-He-Hn-1 clusters to form Va-He-

Hn is calculated by

$$E_{d(H)} = E_{(Fe,Va,He,Hn)} - E_{(Fe,Va,He,Hn-1)} - E_H, \quad (4.2)$$

Where E (Fe,Va,He,Hn) is the total energy of Fe with vacancy, He and n H atoms, and E (Fe,He,Hn-1) is the total energy of perfect Fe with vacancy, He and n-1 H atoms. And the average Ed of H in each cluster is calculated by

$$\bar{E}_{d(H)} = \frac{1}{n}[E_{(Fe,Va,He,Hn)} - E_{(Fe,Va,He)} - nE_H], \quad (4.3)$$

Where E(Fe,Va,He) is the total energy of Fe with vacancy, He but no H atoms.

As seen in Figure 4.4, the average E_d of H increases with increasing the number of H atoms. This suggests that the bigger the cluster size is, the harder it forms. But the E_d of the Nth H strongly depends on the number of H. For example, the E_d of 3rd and 7th H is the local maximum, while the E_d of 4th and 8th H is the local minimum. A cluster with a symmetric structure would have the local minimal value in E_d of Nth H, like Va-He-H_4 and Va-He-H_8. While, the cluster with an asymmetric structure would have the local maximal value in E_d of Nth H, like Va-He-H_3 and Va-He-H_7. When the number of H is up to 8, the E_d of H would still be lower than that of H at T-site in Fe (blue line in Fig. 4). However, when 9 H atoms are put into the structure, one or more H atoms always get out of vacancy. It implies that Va-He-H_8 cannot trap H atom any more. Thus, a Va-He-H_9 can hardly form and the maximal number of H trapped in one Va-He complex is 8.

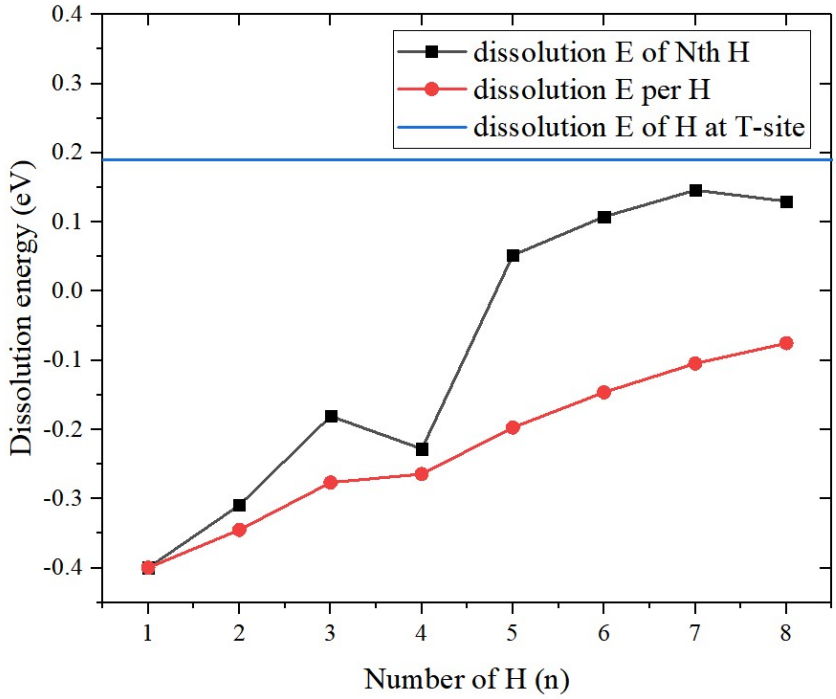

Figure 4.4 The E_d of H in each different Va-He-H_n clusters

Va-He shows stronger ability in trapping H than monovacancy, as the previous study shows the maximal number of H atoms trapped in monovacancy would be 6 [41]. The charge density of monovacancy and Va-He complex are presented in Figure 4.5. The Va-He complex provides an isosurface with low charge density, which H energetically prefers to stay. It is clear that Va-He complex has a bigger volume than monovacancy. This can be one of the reasons why Va-He complex can accommodate more H atoms than monovacancy.

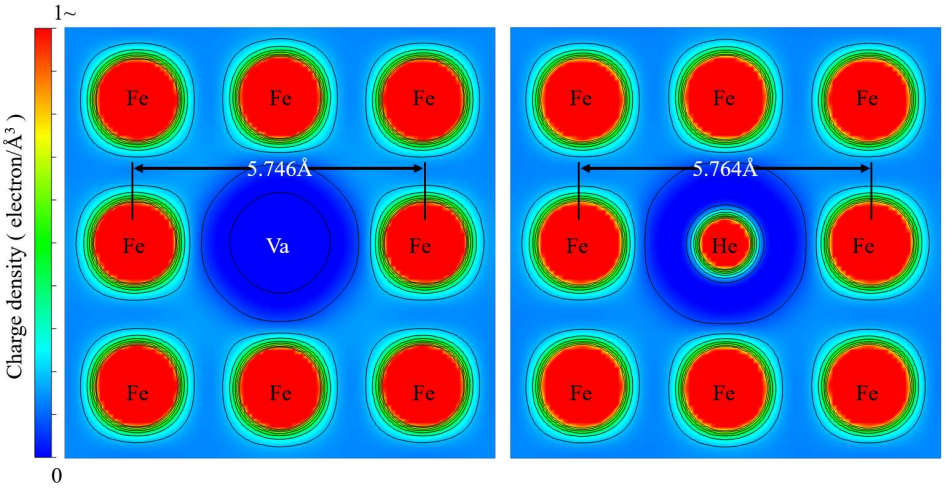

Figure 4.5 Charge density plots of monovacancy and VaHe complex in α Fe

4.6. Summary

In this chapter, the synergistic interaction of H and He in bcc Fe is studied by density functional theory calculation method.

In Fe without vacancy, H and He coexist by staying at different T-sites. The most stable configuration is two T-sites with the distance of 1.94 Å. There is an attractive interaction between H and He in Fe, which is originated from the redistribution of charge density caused by He, and this could drive H segregation towards He.

In Fe with monovacancy, the Va-He complex can trap more H atoms than monovacancy. The maximum number of H trapped in Va-He complex would be 8.

Chapter 5 – Behavior of Hydrogen at Fe/W Interface

5.1. Introduction

Tungsten (W) is one of key materials in fusion engineering field due to its excellent properties, such as high melting point, high strength, low tritium inventory and high resistance against sputtering [56-58]. An amount of research has been devoted to developing W and its alloys [59-61] as the leading candidate materials for the First Wall (FW) in fusion reactor. Recently, W-reduced activation ferritic/martensitic steel (RAFM) composites, which as the concept of FW materials for Fusion Nuclear Science Facility (FNSF) [62], has drawn growing interest in materials research communities [60, 63]. One concern of W-RAFM composite is the irradiation effect on the cohesion properties between W and RAFM, because they would be the critical issue on the security and performance of fusion reactor.

In neutron irradiated metals, Hydrogen (H) and Helium (He) are two typical impurities which are produced due to the transmutation reaction [64]. Previous reports show that both H and He have a significant impact on the mechanical properties of metals [65-67]. For example, the accumulation of H and He in steel will result in the embrittlement. To understand the physical origin of the effect of H and He in W and RAFM steel, the behavior of H and He in W and Fe has been investigated at atomic level by theoretical calculation methods [22, 25-27, 29, 33, 34, 37, 68].

During the fusion process H and He will be abundant in FW materials, so it is necessary to investigate the impact of them on the cohesion between W and RAFM steel. Yang et al. studied the influence of He on the cohesion properties of Fe/W interface [63]. In their work, Fe/W interface is regarded as the model of cohesion of RAFM steel and W, since the primary composition of RAFM steel is Fe. Their results show that in Fe/W interface region, the solution energies of He at Fe side are much smaller than at W side. And, in most cases, He weakens the strength of Fe/W interface. However, there are just few reports about the effects of H on the cohesion of Fe/W interface.

By means of density functional theory (DFT) calculations, this study mainly aims to investigate the stability of H atom at Fe/W interfaces, and effects of H

atom on the strength of Fe/W interface. Also, the behavior of H atom at Fe/W interfaces is compared with the behavior of He atom at Fe/W interfaces.

5.2. Details of Calculations

The density functional calculation in this work is performed by GPAW [69] which is a DFT calculation code implemented in the projector augmented-wave formalism [52]. The generalized gradient approximation (GGA) of Perdew-Burke-Ernzerhof (PBE) [53] is used for exchange-correlation interaction. The sampling of Brillouin zones is with Monkhorst–Pack K-points of 4×4×1. Although there is a huge lattice mismatch (~10%) between Fe and W lattice, it has been confirmed that ultrathin Fe could grow pseudomorphically on W(001) and W(110) in previous experimental studies[70-75]. And, It is reported that Fe(001)/W(001) is thermodynamically more stable than other interfaces [76], so coherent Fe(001)/W(001) is chosen as a typical model for the cohesion of Fe/W. The initial model has five Fe layers and five W layers, each layer is built by a 2×2 (4 atoms) surface unit cell with experimental W lattice 3.16 Å [77]. In the previous studies[25, 27, 63], it has been proved that to study the effect of single point defect, a 2×2 unit supercell is enough to provide reasonable result. After the initial model is built, all atomic positions in initial configuration are relaxed to equilibrium. The relaxed Fe(001)/W(001) is shown in Figure 5.1 (a). After relaxing, the lattice of surface unit cell is changed to 3.10 Å and the spacing between each layer is also changed. Then one H atom is introduced to this interface and atoms is relaxed and energy minimization is continued until the forces on all atoms were converged to less than 5×10^{-2} eV/ Å. Zero point energy (ZPE) corrections are included in all calculation involving H atom by considering ZPE of H has a significant effect on the dissolution energy of H [30]. The ZPE of H is calculated by summing up the zero-point vibrational energies of H's normal modes.

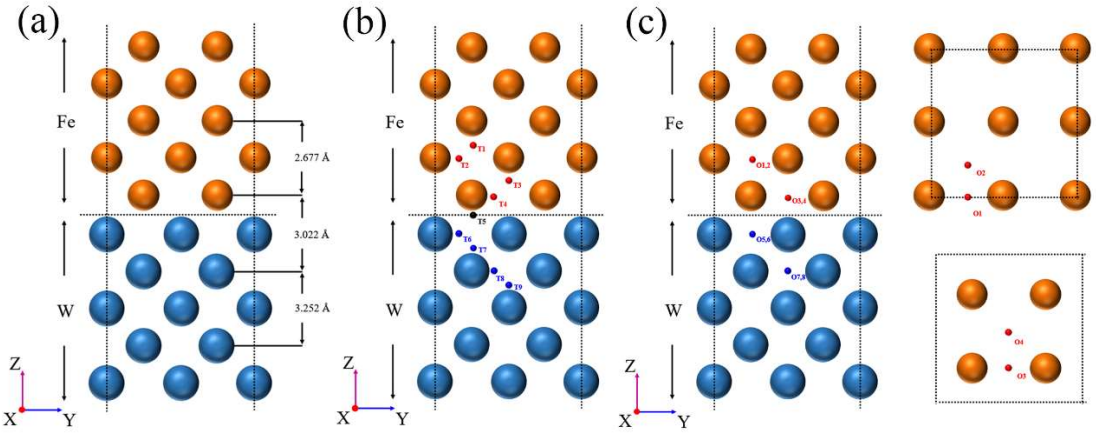

Figure 5.1 Schematic graph of Fe(001)/W(001) interface. (a) relaxed Fe(100)/W(100) interface. (b) the tetrahedral sites (T1-T9) in interface. (c) the octahedral sites (O1-O8) in interface. The orange balls and blue balls represent Fe and W atom, respectively.

5.3. Dissolution Behavior of H Atom at Fe/W Interface

The dissolution of hydrogen atom can be divided into two situations. They are the dissolution of H atom at interstitials site and the dissolution of H atom at vacancy. In general, the dissolution of H at interstitial site in metal shows positive dissolution energy, implying H is energetically unfavorable at interstitial site. While on the contrary, the dissolution of H atom at vacancy shows negative dissolution energy. Therefore, these two situations are studied separately.

5.3.1 H atom at interstitial sites at Fe/W interface

In W bulk and Fe bulk, the possible interstitial sites for small atom are tetrahedral site (T site) and octahedral site (O site) [27, 34, 68]. In this study 9 tetrahedral site and 8 octahedral sites are selected for H. The positions of these T sites and O sites are shown in Figure 5.1(b) and Figure 5.1(c). among them, T1-T4 sites and O1-O4 sites are located in Fe side, T5-T9 sites and O5-O8 sites are located in W side, and T5 is just at the position between Fe and W layers.

The stability of H atom at interstitial sites are investigated by calculating the dissolution energy (E_{dis}) of H at different positions. The calculation of E_{dis} follows formula:

$$E_{dis} = E_{tol} - E_{Fe/W} - E_H \quad (5.1)$$

Where E_{tol} is the total energy of the Fe/W interface with H, $E_{Fe/W}$ is the energy of the Fe/W interface without H and E_H is half energy of a H_2 molecule.

The calculated dissolution energy (E_{dis}) are shown in Figure 5.2. It can be seen that, for both T sites and O sites, the E_{dis} of H increases from Fe side to W side. It indicates that H prefers to stay at Fe side than W side which is similar with the situation in Fe bulk and W bulk [27, 34, 68]. The changing of E_{dis} of H at Fe/W interface is continuous and the former studies [40, 78] show that the diffusion energy of interstitial H is low (0.08 eV in Fe and 0.2 eV in W), So it is considered that H atom could diffuse from W side to Fe side.

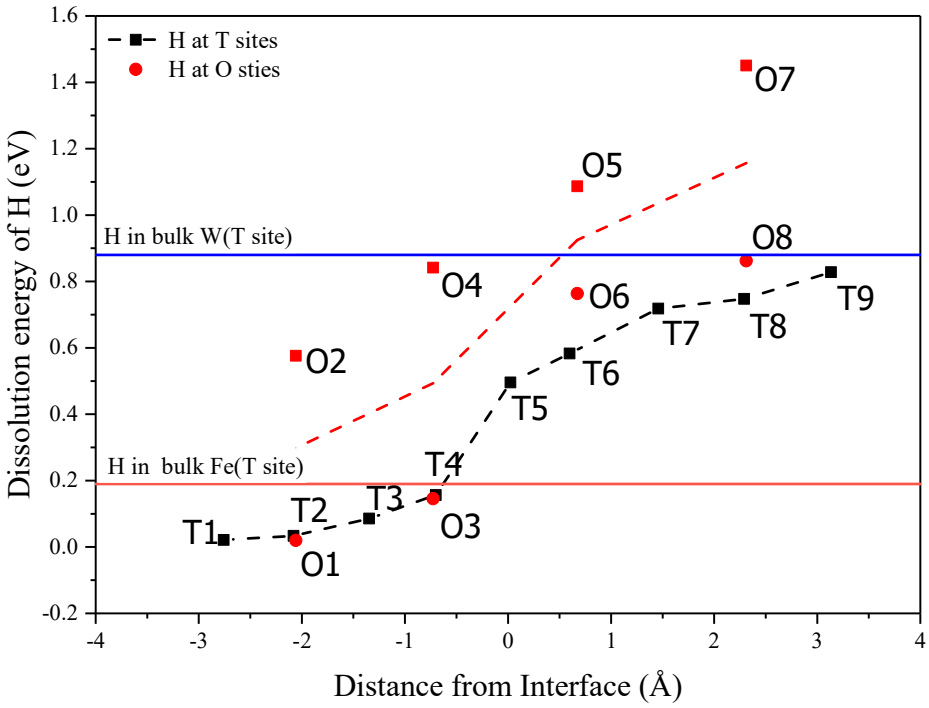

Figure 5.2 The dissolution energy (Edis) of H atom at different interstitial sites in Fe/W interface. 0 in X axis represents central position of interface.

To make a comparison with the situation in Fe and W bulk, the E_{dis} of H atom at T site in Fe bulk and in W bulk are shown by blue line and orange line respectively in Figure 5.2. It is easily to be noticed that, for H at T sites in Fe side in Fe/W interface, the E_{dis} of it is lower than the E_{dis} of H at T sites in Fe bulk, and it has the familiar situation for H at W side. It indicates that Fe/W interface has a sink effect for H since it decreases the E_{dis} of H and makes H become more stable in interface region than in Fe or W bulk.

It has been reported that the E_{dis} of H in metal is proportional to the charge density [55]. It is found there is expansion in lattice within Fe/W interface region. For example, the expansion in Fe side is about 12% compared with Fe bulk. The low charge density in Fe/W interface due to this lattice distortion is considered to be the reason why Fe/W interface decreases the E_{dis} of H.

And, the E_{dis} of H at O sites have greater value than it of H at T sites, which implies that H prefers to stay at T sites at Fe/W interface just like in Fe and W bulk.

5.3.2 H atom trapped in vacancy at Fe/W interface

It has been reported that vacancy (Va) is the trapping site for H atom in both

Fe and W bulk. At first, how Fe/W interface affects the formation of vacancy is studied by calculating the formation energy of monovacancy (E_v). As shown in Figure 5.3(a), 6 monovacancies from Va_1 to Va_6 are selected and the E_v of each was calculated by

$$E_v = E_{Fe/W\ with\ Va} - E_{Fe/W} + E_X \quad (2)$$

Where $E_{Fe/W\ with\ Va}$ is the total energy of the Fe/W interface with Va, $E_{Fe/W}$ is the energy of the Fe/W interface without Va and E_X is the energy of a Fe (or W) atom in bcc Fe (or W) bulk. The results are shown in Figure 5.3(b). For comparison, the E_v in Fe bulk (orange line) and the E_v in W bulk (blue line) are also presented in Figure 5.3 (b). It can be seen that vacancy at Fe side has lower E_v than vacancy at W side, it implies that vacancy is easy to be formed in Fe side of Fe/W interface. After compared E_v in Fe side of Fe/W interface with E_v in Fe bulk, it can be found that interface makes the E_v increases which means that the formation of vacancy at Fe side of Fe/W interface become harder than it in Fe bulk. While interface has the opposite effect for vacancy at W side of Fe/W interface, it decreases E_v and makes the formation of vacancy at W side of Fe/W interface become easier than it at W bulk.

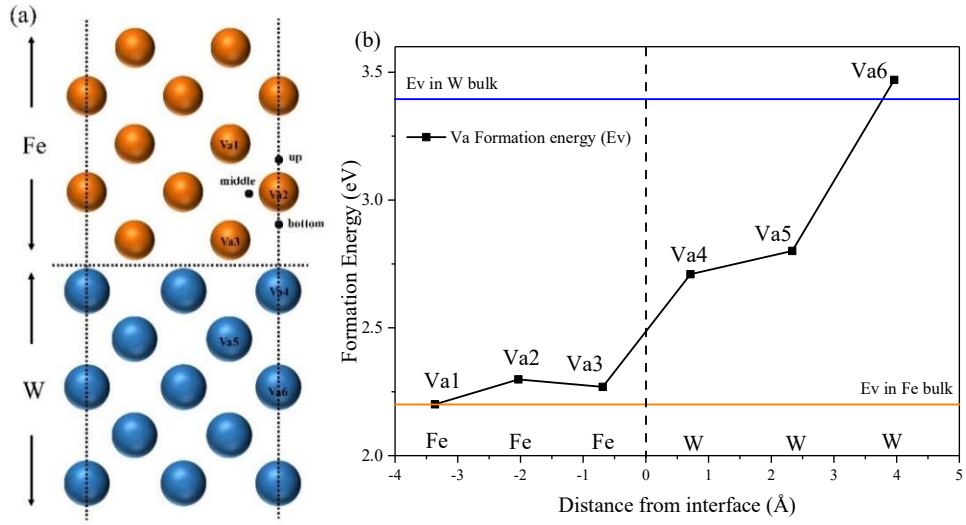

Figure 5.3 Schematic graph of 6 monovacancies at Fe(100)/W(100) interface. (b) formation energy of monovacancy (Ev) at Fe(100)/W(100) interface.

When H is trapped in vacancy, according to the former report, interstitial H atom in Fe or W bulk prefers to stay at a position which is close to O sites[24, 34]. So, when H trapped in the vacancy at Fe/W interface, it has three possible trapping position for each vacancy. For instance, when H is trapped in Va_2, the 3 positions are shown in Figure 5.3 (a) marked as up, middle and bottom. To study the

trapping behavior of H in vacancy, Va_2 – Va_5 are selected since they are close to interface and the E_{dis} of H in vacancy are calculated. The calculation of E_{dis} is similar with before, it follows the formula

$$E_{dis} = E_{tol} - E_{Fe/W+Va} - E_H \quad (5.3)$$

E_{tol} represents the energy of Fe/W interface containing monovacancy and H atom.

The E_{dis} of H in vacancy (Va_2 – Va_5) are within the range of -0.32 to -0.14 eV. And it is found that even in same vacancy, E_{dis} of H is different from site to site and in many cases, H does not stay at the position which is close to O sites. The varied E_{dis} of H and the changed occupation preference of H implies that an special charge density distribution exists inside vacancy, because in pure Fe or W, H prefers to bind onto a sphere isosurface of a certain charge density surrounding the vacancy and has a constant E_{dis} value [36].

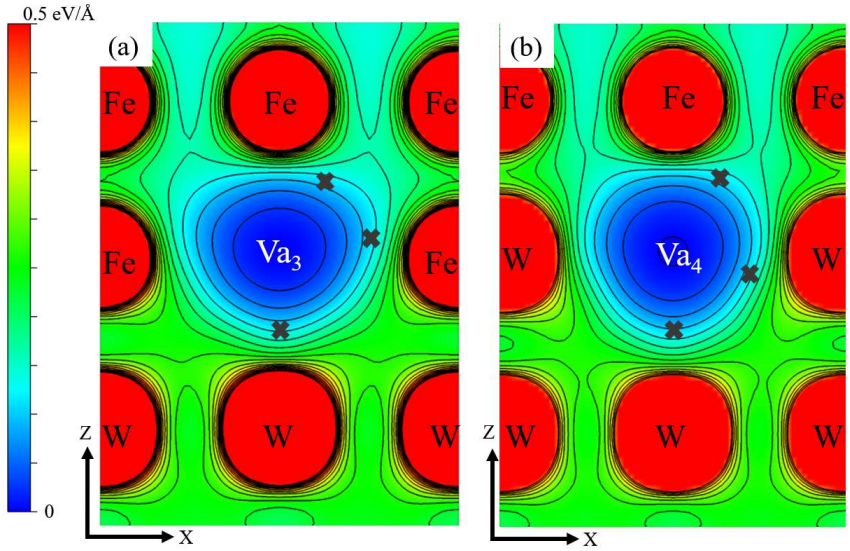

Figure 5.4 The charge density (e/ Å3) of Fe/W interface with (a) Va3 and (b) Va4, and occupation preference of H is marked as ×.

Figure 5.4 shows the charge density map of Va3 and Va4. The charge density distribution in vacancy region at bulk metal is uniform, however, it is obvious that due to the influence of interface, charge density distribution in Va3 and Va4 is no more uniform. The region which close to Fe lattice has a lower charge density compare with the region which close to W lattice. All occupation preference of H in vacancy are marked in Figure 5.4. These occupation sites are considered to be the low energy H binding sites, so it can be found that now there are 9 low energy H binding sites. While there are only 6 low energy H binding sites within one vacancy in bulk Fe or W. and, it is found that the site close to Fe lattice has a

lower E_{dis} of H. Similar charge density distribution also can be found in Va_2 and Va_5, but they are not significant different from normal vacancy as Va_3 and Va_4, which may because they are far away from interface compare with Va_3 and Va_4. It is also noticeable that, although at interface region, charge density inside a vacancy changed, in all cases E_{dis} of H in vacancy still has negative value, it means that vacancy at Fe/W interface remains the trapping site for H atom.

Fe atoms at Fe/W interface show special magnetism. Table 5.1 presents the magnetic moment of Fe atoms and W atoms which are the closest to Fe/W interface. The magnetic moment of Fe atoms and W atoms at defect free interface are calculated to be $1.83\mu_B$ and $-0.2\mu_B$, respectively. It is in agreement with previous study [79]. The magnetic moment of W atoms has no significant changing in all cases, so only the magnetic moment of W atoms at defect free interface is presented. Comparing the magnetic moment of Fe atoms at Fe/W interface with/without H atoms, it appears that the magnetic moment of Fe could be enhanced by H atom. When there is vacancy, the magnetic moment of Fe near vacancy is reduced significantly (Fe_2 and Fe_3 in table 1), but an increasing in magnetic moment of Fe which far away from vacancy is found (Fe_1 in table 1).

Table 5.1. Magnetic moments(μ_B) for Fe layer and W layer at Fe/W interface

Fe/W interface	Fe/W interface	Fe/W interface with H at T5	Fe/W interface with vacancy	Fe/W interface with vacancy-H complex
Fe_1(1.83)	W_1(-0.20)	Fe_1(1.88)	Fe_1(1.99)	Fe_1(2.12)
Fe_2(1.83)	W_2(-0.20)	Fe_2(1.88)	Fe_2(1.39)	Fe_2(1.51)
Fe_3(1.83)	W_3(-0.20)	Fe_3(1.97)	Fe_3(1.39)	Fe_3(1.51)
Fe_4(1.83)	W_4(-0.20)	Fe_4(1.97)	Va_3	Va_3-H

5.4. Effect of H Atom on the Cohesion Properties of Fe/W Interface

The strength of Fe/W interface is expressed by the separation work of Fe/W interface which is the energy needed to completely separate Fe/W interface into Fe parts and W parts [63, 76]. The separation work (W_{sep}) of Fe/W interface is calculated as formula:

$$W_{sep} = \frac{E_{Fe} + E_W - E_{tol}}{A} \quad (5.4)$$

Where E_{Fe} and E_W are the energy of Fe part and W part after the interface is completely separated into two parts. E_{tol} is the energy of Fe/W interface and A is

the surface area of the interface.

Figure 5.5 (a) shows the W_{sep} of Fe/W interface containing H atom at different sites, it can be found that H atom at all sites except O8 could decrease the W_{sep} of Fe/W interface. This is similar with the case of He [63], however, the effect of H is really limited compared with He, since He could lead a 1.5 J/m^2 decreasing in W_{sep}, while H only could lead a 0.56 J/m^2 decreasing(O4 in Figure 5.5 (a)). It is noticeable that H at O8 site could slightly increase the W_{sep} of interface. Figure 5.6 (b) shows the W_{sep} of Fe/W interface containing vacancy or vacancy-H complex. Vacancy could strongly decrease the W_{sep} compared with H atom. And Vacancy-H complex apparently has similar effect as vacancy on decreasing the W_{sep} of Fe/W interface. It implies that vacancy plays the main role in vacancy-H complex to decrease the strength of Fe/W interface.

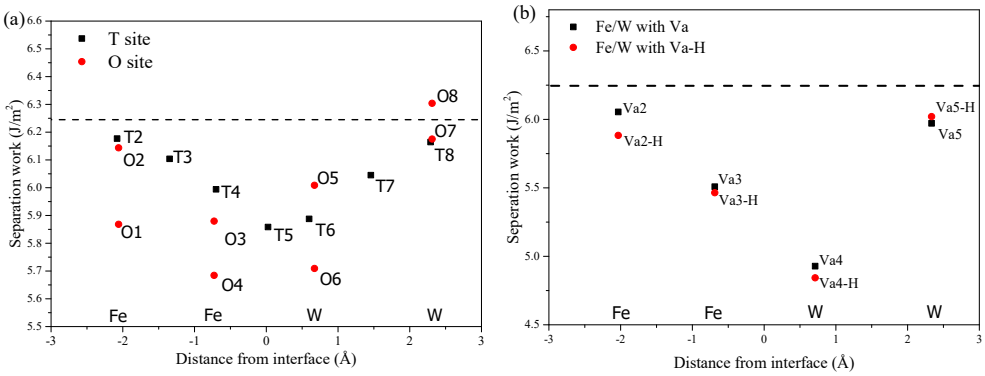

Figure 5.5 The separation work of Fe/W interfaces with (a) H, (b) vacancy and vacancy-hydrogen complex.

To understand the effects of H atom and vacancy on the cohesion of Fe/W interface. The charge density of Fe/W interface with and without vacancy, and Fe/W interface with H at O4 and O8 site are analyzed. Figure 5.6 (a) shows the charge density of Fe/W interface and Figure 5.6 (b) shows the charge density of Fe/W interface with vacancy. By comparing these two figures, it is clear that vacancy eliminates the bonds between Fe and W atom. This is considered as the main reason why vacancy is harmful to the strength of Fe/W interface. Figure 5.6 (c) and Figure 5.6 (d) show the cases of Fe/W interface with H at O4 and O8 site. It is noticeable that H does bond with both Fe and W. However, there is no evidence to show that this bond provides an additional strength of interface. It is believed that the influence of H on strength of interface mainly due to the strain which caused by H. For example, it can be seen that when H is at O4 site (Figure 5.6 (c)), it obviously increases the distance between Fe and W atom and

consequently decreases the charge density as well as the bond strength between Fe and W. on the contrary when H is at O8 site (Figure 5.6 (d)), it pushes the W atom close to Fe atom and consequently increases the charge density as well as the bond strength between Fe and W. And, As discussed in Figure 5.5 (b), vacancy-H complex almost has the same effect as vacancy on the strength Fe/W interface, which can be explain as that after dissolve a H atom in vacancy there is no obvious changing in the strain, because vacancy could provide enough space for H atom.

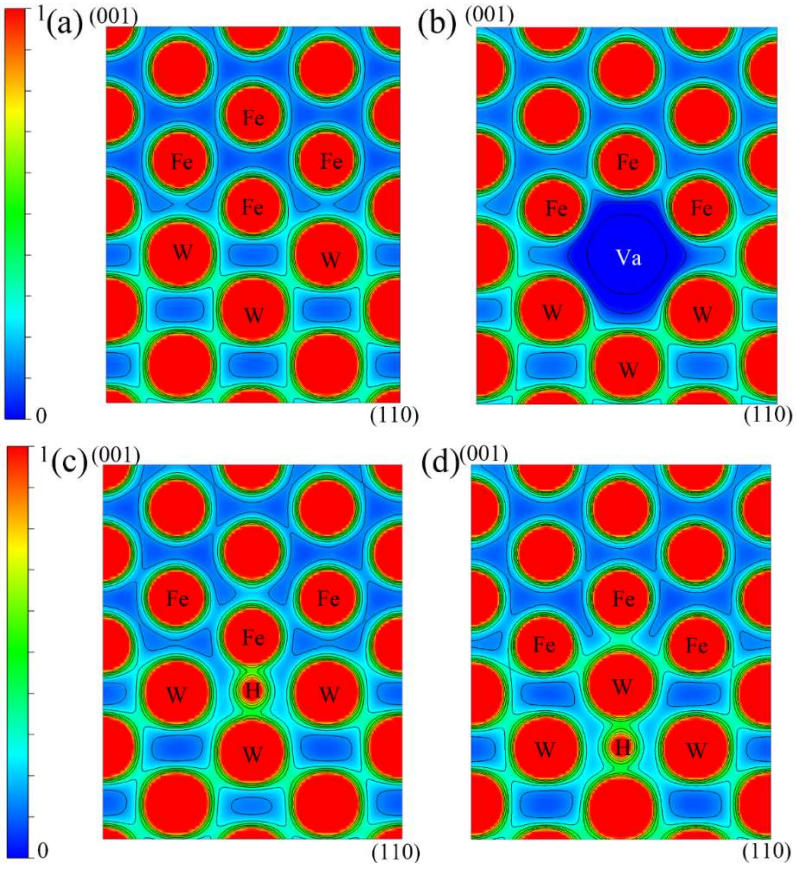

Figure 5.6 The charge density (e/ Å^3) of Fe/W interface with (a) no defect, (b) vacancy, (c) H atom at O4 site and (d) H atom at O8 site.

5.5. Summary

In this chapter, the dissolution behavior of hydrogen at Fe/W interface and the effect of hydrogen on the strength of Fe/W interface are investigated by means of first principle calculation. The dissolution of H at Fe/W interface seems to be easier than that at Fe or W bulk, due to the distortion within Fe/W interface region. It suggested that Fe/W interface would have a sink effect for H atom. The effect of H on the strength of Fe/W interface would be mainly due to its influence on bond strength between Fe and W. On the other hand, vacancy would have negative influence on the strength of interface probably due to the elimination of the bond between Fe and W.

Chapter 6 – Cohesion Properties of incoherent Fe/W interface

6.1. Introduction

For the past decades, Fe/W interfaces have been drawn much attention of researchers[73, 74, 80-86], mostly due to its interesting magnetic properties which can be easily modified by changing the parameters in preparation such as growth conditions, thickness of Fe layer. It has been reported that the first monolayer of Fe could pseudomorphically grow on both W(001) and W(110)[87] despite there is a huge mismatch between Fe and W lattice. And some theoretical works have devoted to studying these coherent Fe/W interfaces[76, 88].

For fusion reactor, tungsten is considered as the most promising candidate for plasma facing materials (PFMs) used in the first wall [89]. However, single W still barely satisfied the future fusion reactor like The US Fusion Nuclear Science Facility (FNSF) [62], since PFMs for fusion reactor have to tolerate more severe thermal, physical and mechanical loads. Therefore, metallic multilayers have been proposed as promising materials that can be used as the PFMS in future fusion nuclear reactors [90]. Very recently, several works made effort to develop W-Fe composite materials as the candidate for PFMs [60, 91, 92]. Due to the huge difference in lattice between Fe (2.87 Å) and W(3.16 Å), the Fe/W interfaces exist in these W-Fe composite should be considered as incoherent Fe/W interface.

For all the above reasons, the incoherent Fe/W interface deserves to be studied. Theoretical simulations should be performed to study the cohesion properties of incoherent Fe/W interface, as they play important role in the performance and lifetime of W-Fe composite materials. In this work, density functional theory (DFT) calculations are performed to investigate the interface energy and strength of incoherent Fe/W interfaces.

6.2. Details of Calculations

Density functional theory (DFT) calculations are performed with GPAW [52], a density-functional theory (DFT) Python code based on the projector-augmented wave (PAW) method. The Perdew-Burke-Ernzerhof (PBE) [53] GGA functional is employed to describe the exchange-correlation. In this work,

Fe(100)/W(100), Fe(110)/W(110) and Fe(100)/W(110) three Fe/W interfaces are studied. Each interface consists of 5 Fe layers and 5 W layers where the top two layers of Fe and the bottom two layers of W are fixed by maintaining the ideal bulk structure. The difference in lattice between Fe (2.84 Å) and W(3.16 Å) could result in more than 10% mismatch. To make sure the mismatch in created Fe/W interfaces keeps a small value, Fe(100)/W(100) and Fe(110)/W(110) interfaces are built with 7 x 7 Fe surface unit cell and 6 x 6 W surface unit cell and Fe(100)/W(110) is built with 8 x 8 Fe surface unit cell and 7 x 5 W surface unit cell. The mismatch of these three interfaces is about 4%. To determine the stable configuration, the initial intersurface distance between Fe and W is varied from 1.5 Å to 4 Å. The interfaces are relaxed until the atomic force is less than 0.05 eV/ Å. Due to the large size of supercell, only Γ point is used in relaxed calculation.

6.3. The Structure of Fe(100)/W(100), Fe(110)/W(110) and Fe(100)/W(110) Interfaces

First of all, the stability of Fe(100)/W(100), Fe(110)/W(110) and Fe(100)/W(110) three Fe/W interfaces is investigated. Interface energy (E_{int}) is adopted as the criterion to describe interface stability. Usually, higher interface energy means less stable interface and vice versa. The interface energies of Fe(100)/W(100), Fe(110)/W(110) and Fe(100)/W(110) interfaces with different initial intersurface distance are calculated using the following equation:

$$E_{int} = \frac{E_{tol} - E_{Fe\_bulk} - E_{W\_bulk}}{A} \quad (6.1)$$

where E_{tot} is the total energy of the interface and A is the interface area, E_{Fe_bulk} and E_{W_bulk} are bulk energies of pure Fe and W layers, respectively. The calculated E_{int} is shown in Figure 6.1.

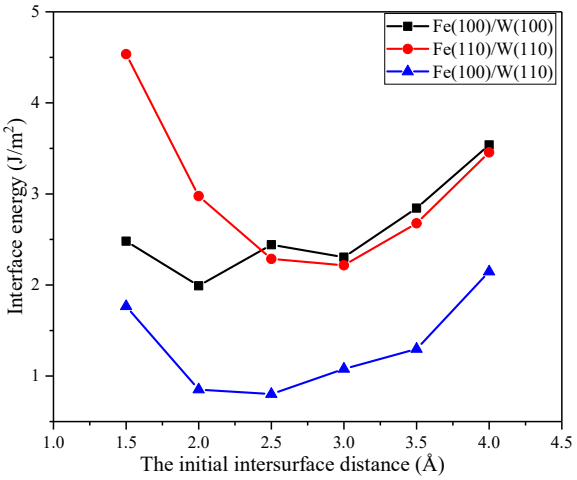

Figure 6.1 The interface energy of Fe/W interfaces with various initial intersurface distance.

It can be found that the interface energies of all three Fe/W interface have a positive value, and the interface energies of these three Fe/W interface are higher than that of coherent Fe/W interfaces [76]. It means that the thermal stability of incoherent Fe/W interface is lower than the coherent Fe/W interfaces. And the most possible reason is that the strain at incoherent interface is larger than it at coherent interface. Among these three interfaces, Fe(100)/W(110) interface has the lowest interface energy, indicating that it has the highest thermal stability. Interface energy of Fe(100)/W(100) interface is slightly lower than that of Fe(110)/W(110) interface, which is consistent with the former report [76]. It is considered that the interface energy of Fe/W interfaces has strong correlation with the lattice structure in interface region. Thus, it is necessary to check the configuration of Fe/W interfaces in detail.

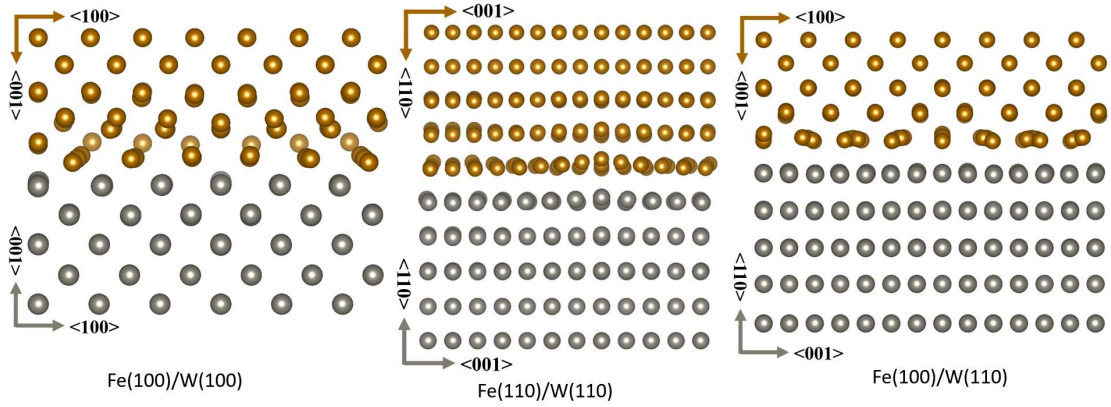

Figure 6.2 The lateral view of Fe(100)/W(100), Fe(110)/W(110) and

Fe(100)/W(110) interfaces. Orange balls represent Fe atoms and grey balls represent W atoms.

Figure 6.2 shows the relaxed configuration of Fe(100)/W(100), Fe(110)/W(110) and Fe(100)/W(110) interfaces with lowest interface energy. In all three interfaces, there is no mixing of Fe and W is found, which is consistent with the experimental works [73, 83, 86]. And it is noticeable that in all three interfaces an obvious reconstruction can only be observed in Fe lattice. It could be explained in terms of elasticity, since W has a much higher bulk modulus (315 GPa) than Fe (170 GPa) and the consequently higher energy cost to deform W lattice. Apparently, Fe(100)/W(100) interface shows the strongest reconstruction, the lattice of the first Fe layer and second Fe layer are obviously disordered. While the reconstruction in Fe(110)/W(110) interface is weaker than it in Fe(100)/W(100) interface, the disorder in lattice is obvious in first Fe layer but it is limited in the second Fe layer. The reconstruction in Fe(100)/W(110) interface is the weakest, the obvious disorder in lattice can only be found in the first Fe layer. It is believed that the limited disorder in Fe(100)/W(110) interface could explain the lowest interface energy of Fe(100)/W(110) interface.

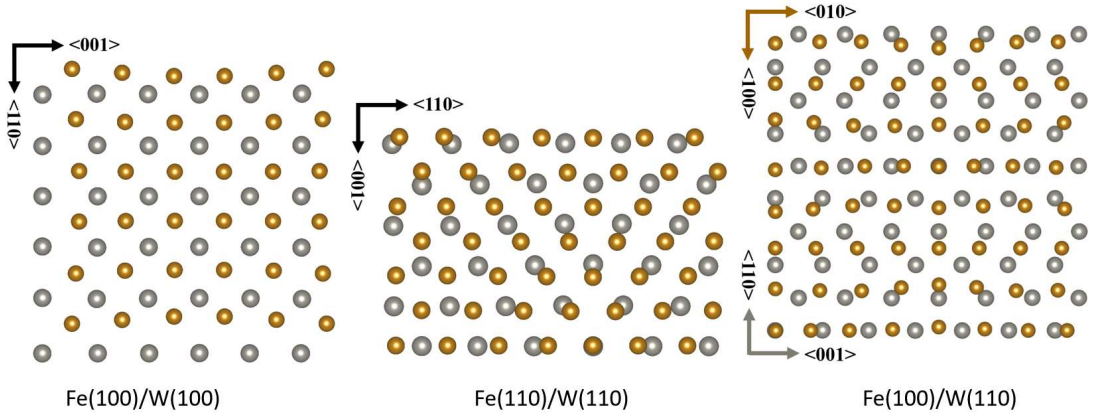

Figure 6.3 The frontal view of Fe layer and W layer that contacted each other in Fe(001)/W(001), Fe(110)/W(110) and Fe(001)/W(110) interfaces. Orange balls represent Fe atoms and grey balls represent W atoms.

In addition, to investigate the configuration of Fe/W interfaces in more detail, the configuration of the Fe layer and the W layer that contacted each other are checked, as shown in Figure 6.3. Interestingly, in Fe(001)/W(001) interface Fe layer with a pseudomorphic structure formed, this result has good agreement with the former experimental reports [73, 83]. However, no such configuration is observed in Fe(110)/W(110) and Fe(001)/W(110) interfaces.

6.4. The strength of Fe(100)/W(100), Fe(110)/W(110) and Fe(100)/W(110) Interfaces

The strength of interface is an important cohesion property of interface. To evaluate the strength of Fe/W interfaces, the separation work (W_{sep}) of interface is calculated with the following equation:

$$W_{sep} = \frac{E_W + E_{Fe} - E_{tot}}{A} \tag{6.2}$$

where E_{tot} is the total energy of the interface and A is the interface area, E_{Fe} and E_W are energies of Fe layers and W layers which are completely separated, respectively. Results are shown in Figure 6.4. It can be seen that Fe(110)/W(110) interface has the highest W_{sep}, indicating it has the highest strength, followed by Fe(100)/W(100) interface and Fe(100)/W(110) interface.

To discuss the strength of interfaces from the fundamental interaction between Fe atom and W atom, the bond energy of Fe-Fe, W-W and Fe-W is calculated, as shown in Figure 6.4(b). Obviously, W-W bond is strongest with the lowest bond energy than Fe-W bond and Fe-Fe bond. this result implies the strong interaction between Fe and W and this could be another reason to explain why reconstruction mainly happened in Fe lattice. And an important information here is that the bond energy of Fe-W shows negative value, which means that an attractive interaction exists between Fe atom and W atom. In Figure 6.4 (a), Fe(110)/W(110) interface shows the strongest strength, which may mainly be due to that the number of Fe-W bonds in Fe(110)/W(110) interface is the largest, since (110) plane has more atoms than other planes with the same area.

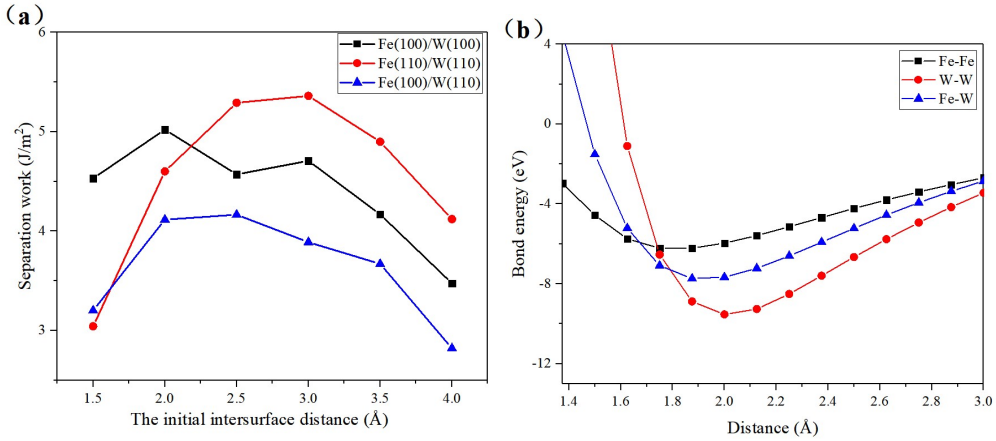

Figure 6.4 The separation work of Fe/W interfaces with various initial intersurface distance. (b) The bond energy of Fe-Fe, W-W and Fe-W atoms.

6.5. The electronic structure and magnetism of Fe(100)/W(100), Fe(110)/W(110) and Fe(100)/W(110) Interfaces

The electronic structure of Fe/W interfaces is investigated to have a fundamental understanding of the cohesion of Fe/W interfaces. Figure 6.5(a) shows the density of states (DOS) of Fe(001)/W(001), Fe(110)/W(110) and Fe(001)/W(110) interfaces. The DOS of these three interfaces doesn't show much difference in the bandwidth. What is noticeable is that compared with Fe(001)/W(001) and Fe(001)/W(110) interfaces, the DOS of Fe(110)/W(110) interface has more distribution with high values DOS peaks, implying that strong chemical bond exists in Fe(110)/W(110) interface. It could be one reason why Fe(110)/W(110) interface shows the strongest strength. The DOS of Fe(001)/W(001) interface has slightly bigger binding energies than DOS of Fe(001)/W(110) interface. It means the bond in Fe(001)/W(001) interface is stronger than it in Fe(001)/W(110) interface, which is consistent with that Fe(001)/W(001) interface has higher Wsep than Fe(001)/W(110) interface. Also, the charger transfer in Fe/W interfaces is analyzed by Bader analysis [93-95]. Results show that not like in the coherent Fe/W interface, an obvious charger transfer is not found in the incoherent Fe/W interfaces, which has an agreement with the former report [96].

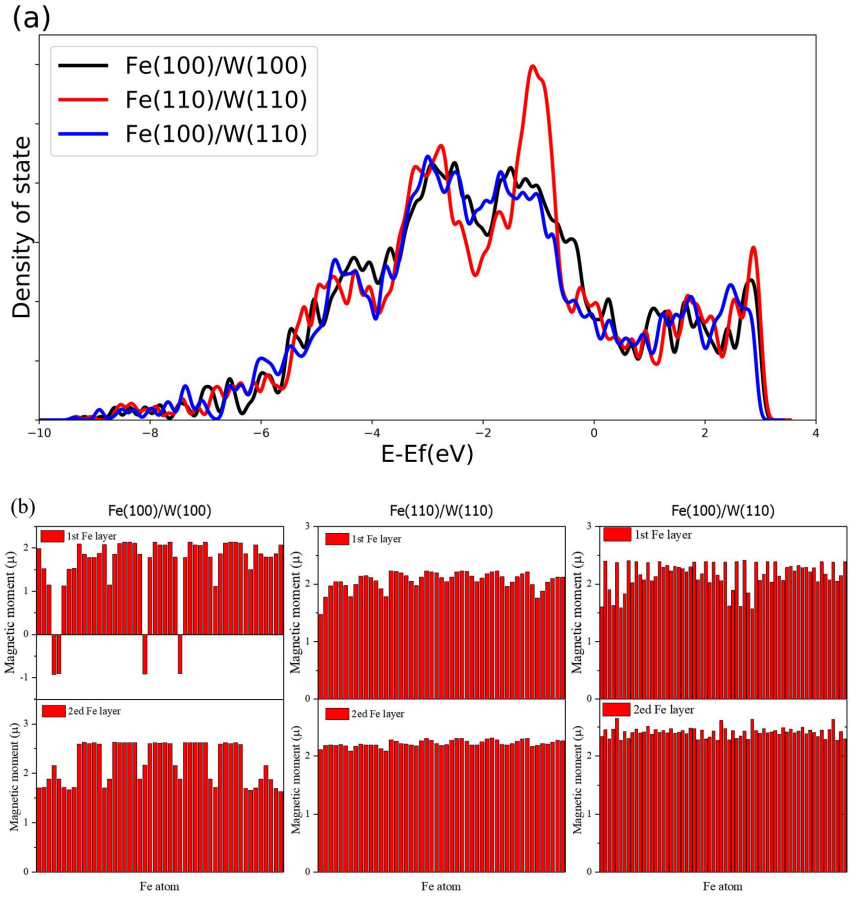

Figure 6.5 (a) Density of states (DOS) of Fe/W interfaces. (b) magnetic moment of Fe at 1st Fe layer and 2ed Fe layer of Fe/W interfaces.

Furthermore, since many researches have reported that the magnetism of Fe layers at Fe/W interface is very different from bulk Fe. The magnetic moment of Fe at the 1st Fe layer and 2ed Fe layer of Fe/W interfaces are presented in Figure 6.5(b). For comparison the magnetic moment of Fe atom in bulk is calculated to be 2.24 μ which is consistent with former study [27]. From Figure 6.5(b), it can be found that the magnetic moment of Fe at the 1st Fe layer of Fe/W interface is quite different from it of Fe at bulk. the reduction in magnetic moment of Fe at the 1st Fe layer is obvious, especially in the 1st Fe layer at Fe(100)/W(100) interface, every magnetic moment of Fe is less than 2.24 μ and even some Fe atom show opposing magnetic moment (negative value). For Fe(110)/W(110) and Fe(100)/W(110) interfaces, the magnetic moment of Fe at the 2ed Fe layer shows a less variety and the value of magnetic moment becomes close to 2.24 μ. However, for Fe(100)/W(100) interface, the magnetic moment of Fe at the 2ed Fe still be very special. It is considered that it is due to the pseudomorphic structure

in Fe(100)/W(100) interface.

6.6. Monovacancy at Fe(100)/W(100), Fe(110)/W(110) and Fe(100)/W(110) Interfaces

To give a glance on the irradiation behavior of Fe/W interfaces, the formation energy of monovacancy at Fe/W interfaces is investigated. Due to the reconstruction of Fe/W interfaces, the formation of monovacancy could be different from site to site at Fe/W interface. So for each interface, formation energy of monovacancy at three different sites in 1st Fe layer and three different sites in 1st W layer are calculated and presented in Figure 6.6. The formation energy of monovacancy at Fe bulk and W bulk is 2.18 eV and 3.6 eV respectively [97]. Compared with these two values, one can find that the formation energy of monovacancy at 1st Fe layer and 1st W layer of all three Fe/W interfaces is lower, which suggests that the formation of monovacancy in Fe/W interfaces is easier than in bulk Fe or W.

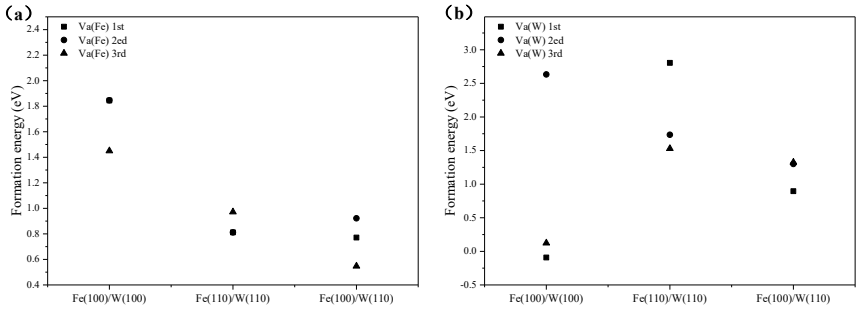

Figure 6.6 The formation energy of monovacancy at (a) 1st Fe layer and (b) 1st W layer of Fe/W interfaces.

And as expected, the formation energy of monovacancy at different sites is quite different. For each Fe/W interface, the difference in formation energy of monovacancy at different sites in Fe lattice is from 0.2 eV to 0.5 eV, while the difference in formation energy of monovacancy at different sites in W lattice is much larger, it could be more than 2.5 eV. Even in Fe(001)/W(001) interface, the formation energy of monovacancy could be negative. It is of interest to check the configuration which the formation of monovacancy in W lattice is negative. That configuration which is Fe(001)/W(001) interface with vacancy in W lattice is shown in Figure 6.7, Figure 6.7 (a) is the configuration before relax and Figure 6.7 (b) is the configuration after relax. It can be seen that when there is a vacancy in W lattice, after relax Fe atom could enter the vacancy position. This reconstruction results in the low formation energy of monovacancy in W lattice,

it also suggests that once vacancy form in W lattice, Fe atom could diffuse to W lattice.

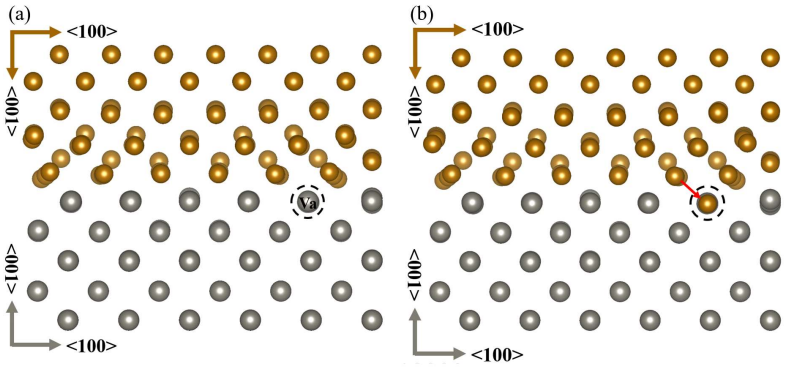

Figure 6.7 The lateral view of Fe(001)/W(001) interface with vacancy in W lattice (a) Before relax. (b) after relax.

6.7. Summary

In this chapter, Density functional theory calculation has been performed to investigate the cohesion properties of three incoherent Fe/W interfaces, Fe(100)/W(100), Fe(110)/W(110) and Fe(100)/W(110) interfaces. It is found that Fe(100)/W(110) interface has the lowest interface energy, followed by Fe(100)/W(100) and Fe(110)/W(110) interfaces. For all three Fe/W interfaces obvious lattice disorder only can be found in Fe lattice. And the lattice disorder in Fe(100)/W(100) interface is most severe, even a pseudomorphic structure formed at the Fe layer in Fe(100)/W(100) interface. While lattice disorder in Fe(100)/W(110) interface is the weakest. Fe(110)/W(110) interface shows the strongest strength, it may be mainly due to the number of Fe-W bonds in Fe(110)/W(110) interface is more than other planes with same area. DOS also shows that compared with other two interfaces, a stronger chemical bond formed in Fe(110)/W(110) interface. Fe at Fe(100)/W(100) interface shows a very abnormal magnetism. In Fe/W interfaces, the formation of monovacancy could be easy than it in bulk Fe or W. and the results also suggest that Fe atom could migrate into W lattice if there is vacancy exist in W lattice.

Chapter 7 – General Conclusions

The behavior of point defects in Fe and Fe-based composite materials are studied. Instead of experiment investigation, theoretical calculation is adopted to focus on the fundamental properties of point defects (vacancy, H and He).

At first, the synergistic effect of hydrogen and helium in α-Fe is investigated using density functional theory calculation method. In perfect crystal of Fe, the presence of helium atom would decrease the dissolution energy of hydrogen atom near helium atom. This implies the existence of an attractive interaction between hydrogen and helium atoms. It is also revealed that the most stable places for both hydrogen and helium atoms are two tetrahedral sites (T-site) with a distance of 2.16 Å. Furthermore, a vacancy-helium complex (Va-He) would be an effective trapping site for hydrogen atom compared with mono-vacancy, a Va-He would be able to trap 8 hydrogen atoms.

Next, the dissolution behavior of hydrogen (H) at Fe/W interface and the effect of H on the strength of Fe/W interface is investigated. The dissolution of H atom at Fe/W interface would be easier than that in bulk of Fe or W due to the low charge density at Fe/W interface by the distortion of lattice. Hydrogen atom is expected to diffuse to Fe side of Fe/W interface due to its lower dissolution energy in Fe lattice at interface. While H atom could be trapped by vacancy at Fe/W interface. In addition, H and vacancy reduce the strength of interface, however, H atom at a special site seems to slightly increase the strength of interface. Furthermore, the electronic structures of interface are analyzed to give a physical understanding on the effect of H on Fe/W interface.

At last, The cohesion properties of three incoherent Fe/W interfaces, Fe(100)/W(100), Fe(110)/W(110) and Fe(100)/W(110) interfaces are investigated. It is found that Fe(100)/W(110) interface has the lowest interface energy, followed by Fe(100)/W(100) and Fe(110)/W(110) interfaces. For all three Fe/W interfaces, obvious lattice disorder only can be found in Fe lattice. And the lattice disorder in Fe(100)/W(100) interface is most severe, even a pseudomorphic structure formed at the Fe layer in Fe(100)/W(100) interface. While lattice disorder in Fe(100)/W(110) interface is the weakest. Fe(110)/W(110) interface shows the strongest strength, it may be mainly due to the number of Fe-W bonds in Fe(110)/W(110) interface is more than other planes with same area. DOS also shows that compared with other two interfaces, a stronger chemical bond formed in Fe(110)/W(110) interface. Fe at Fe(100)/W(100) interface shows a very abnormal magnetism. In Fe/W interfaces,

the formation of monovacancy could be easy than it in bulk Fe or W, and the results also suggest that Fe atom could migrate into W lattice if there is vacancy exist in W lattice.

References

[1] V. Knapp, D. Pevec, Promises and limitations of nuclear fission energy in combating climate change, Energy Policy, 120 (2018) 94-99.

[2] I. Medhaug, M.B. Stolpe, E.M. Fischer, R. Knutti, Reconciling controversies about the 'global warming hiatus', Nature, 545 (2017) 41.

[3] A. De Ninno, A. FRATTOLILLO, A. RIZZO, E. DEL GIUDICE, G. PREPARATA, Experimental evidence of 4He production in a cold fusion experiment, ENEA-Unita Tecnico Scientfica Fusione Centro Ricerche Frascati, (2002).

[4] S.J. Zinkle, J.T. Busby, Structural materials for fission & fusion energy, Materials Today, 12 (2009) 12-19.

[5] E. Moses, R. Boyd, B. Remington, C. Keane, R. Al-Ayat, The National Ignition Facility: Ushering in a new age for high energy density science, Physics of Plasmas, 16 (2009) 041006.

[6] N. Holtkamp, The status of the ITER design, Fusion Engineering and Design, 84 (2009) 98-105.

[7] T. Zhu, S. Jin, Y. Gong, E. Lu, L. Song, Q. Xu, L. Guo, X. Cao, B. Wang, The influence of dislocation and hydrogen on thermal helium desorption behavior in Fe9Cr alloys, Journal of Nuclear Materials, 495 (2017) 244-248.

[8] M.Z. Zhao, P.P. Liu, Y.M. Zhu, F.R. Wan, Z.B. He, Q. Zhan, Effects of hydrogen isotopes in the irradiation damage of CLAM steel, Journal of Nuclear Materials, 466 (2015) 491-495.

[9] Q. Xu, T. Yoshiie, K. Sato, Effects of hydrogen and helium produced by transmutation reactions on void formation in copper isotopic alloys irradiated with neutrons, Journal of Nuclear Materials, 386-388 (2009) 363-366.

[10] M. Shimada, Y. Hatano, Y. Oya, T. Oda, M. Hara, G. Cao, M. Kobayashi, M. Sokolov, H. Watanabe, B. Tyburska-Püschel, Y. Ueda, P. Calderoni, K. Okuno, Overview of the US–Japan collaborative investigation on hydrogen isotope retention in neutron-irradiated and ion-damaged tungsten, Fusion Engineering and Design, 87 (2012) 1166-1170.

[11] R. Ramachandran, C. David, P. Magudapathy, R. Rajaraman, R. Govindaraj, G. Amarendra, Study of defect complexes and their evolution with temperature in hydrogen and helium irradiated RAFM steel using positron annihilation spectroscopy, Fusion Engineering and Design, 142 (2019) 55-62.

[12] J. Morisawa, M. Kodama, N. Yokota, K. Nakata, K. Fukuya, S. Shima, K. Asano, Hydrogen analysis and slow strain rate test in Ar gas for irradiated austenitic stainless steel, Journal of Nuclear Materials, 294 (2001) 241-249.

[13] Y.E. Kupriiyanova, V.V. Bryk, O.V. Borodin, A.S. Kalchenko, V.N. Voyevodin, G.D. Tolstolutskaya, F.A. Garner, Use of double and triple-ion irradiation to study the influence of high levels of helium and hydrogen on void swelling of 8–12% Cr ferritic-martensitic steels, Journal

of Nuclear Materials, 468 (2016) 264-273.

[14] D. Brimbal, L. Beck, M. Payet, F. Jomard, The synergistic effect of hydrogen and helium implantations in forming H2 molecules in a Fe-12 wt.%Cr-ODS steel characterized by Raman spectroscopy and SIMS, Nuclear Instruments and Methods in Physics Research Section B: Beam Interactions with Materials and Atoms, 461 (2019) 191-196.

[15] R. Zhang, H. Zhou, J. Yu, W. Han, M. Liu, C. Chen, K. Zhu, Effect of vanadium alloying on irradiation performance of tungsten under 60 keV helium irradiation, Journal of Nuclear Materials, 512 (2018) 65-71.

[16] B.N. Singh, A. Horsewell, M. Eldrup, F.A. Garner, Fission neutron irradiation of copper containing implanted and transmutation produced helium, Journal of Nuclear Materials, 191-194 (1992) 1259-1264.

[17] T. Sato, T. Okita, N. Sekimura, Effects of solid transmutation and helium on microstructural evolution in neutron-irradiated vanadium, Journal of Nuclear Materials, 307-311 (2002) 385-388.

[18] B. Li, Z. Wang, K. Wei, T. Shen, C. Yao, H. Zhang, Y. Sheng, X. Lu, A. Xiong, W. Han, Evaluation of helium effect on irradiation hardening in F82H, ODS, SIMP and T91 steels by nano-indentation method, Fusion Engineering and Design, 142 (2019) 6-12.

[19] V. Krsjak, J. Degmova, J.S. Veternikova, C.F. Yao, Y. Dai, Experimental comparison of the (ODS)EUROFER steels implanted by helium ions and irradiated in spallation neutron target, Journal of Nuclear Materials, 523 (2019) 51-55.

[20] S. Gavarini, J. Baillet, N. Millard-Pinard, V. Garnier, C. Peaucelle, X. Jaurand, C. Bernard, R. Rapegno, S. Cardinal, C. Dalverny, B. Lanfant, Y. Leconte, Effects of helium irradiation on fine grained β-SiC synthesized by spark plasma sintering, Journal of the European Ceramic Society, 40 (2020) 1-11.

[21] R. Coppola, M. Klimenkov, A. Möslang, R. Lindau, M. Rieth, M. Valli, Micro-structural effects of irradiation temperature and helium content in neutron irradiated B-alloyed Eurofer97-1 steel, Nuclear Materials and Energy, 17 (2018) 40-47.

[22] P. Zhang, J. Ding, D. Sun, J. Zhao, First-principles study of noble gas atoms in bcc Fe, Journal of Nuclear Materials, 492 (2017) 134-141.

[23] J. Ding, P. Zhang, X. Li, Y. Wang, S. Huang, J. Zhao, Magnetism and energetics for vacancy and helium impurity in Fe-9Cr alloy: A first-principles study, Computational Materials Science, 138 (2017) 267-276.

[24] Y. Yu, Q.-F. Han, Z. Zhou, Y. Ma, S. Jia, Y.-L. Liu, Synergistic interplay between H and He in molybdenum: A first-principles study, Journal of Nuclear Materials, 466 (2015) 194-200.

[25] S. Sakuraya, K. Takahashi, N. Hashimoto, S. Ohnuki, The effect of point defects on diffusion pathway within α-Fe, Journal Of Physics. Condensed Matter: An Institute Of Physics Journal, 27 (2015) 175007-175007.

[26] P. Zhang, C. Zhang, R. Li, J. Zhao, He-induced vacancy formation in bcc Fe solid from first-principles simulation, Journal of Nuclear Materials, 444 (2014) 147-152.

[27] S. Sakuraya, K. Takahashi, S. Wang, N. Hashimoto, S. Ohnuki, Physical properties of α-Fe upon the introduction of H, He, C, and N, Solid State Communications, 195 (2014) 70-73.

[28] P. Zhang, R. Li, J. Zhao, B. Wen, Synergetic effect of H and He with vacancy in vanadium solid from first-principles simulations, Nuclear Instruments & Methods in Physics Research Section B, 303 (2013) 75-80.

[29] Y.-N. Liu, T. Ahlgren, L. Bukonte, K. Nordlund, X. Shu, Y. Yu, X.-C. Li, G.-H. Lu, Mechanism of vacancy formation induced by hydrogen in tungsten, AIP Advances, 3 (2013) 122111.

[30] E. Hayward, C.-C. Fu, Interplay between hydrogen and vacancies in α-Fe, Physical Review B, 87 (2013) 174103.

[31] N. Hashimoto, J. Tanimoto, T. Kubota, H. Kinoshita, S. Ohnuki, Analysis of helium and hydrogen effect on RAFS by means of multi-beam electron microscope, Journal of Nuclear Materials, 442 (2013).

[32] J.X. Yan, Z.X. Tian, W. Xiao, W.T. Geng, Interaction of He with Cu, V, and Ta in bcc Fe: A first-principles study, Journal of Applied Physics, 110 (2011) 013508.

[33] B. Jiang, F.R. Wan, W.T. Geng, Strong hydrogen trapping at helium in tungsten: Density functional theory calculations, Physical Review B, 81 (2010) 134112.

[34] Z. Hong-Bo, L. Yue-Lin, J. Shuo, Z. Ying, G.N. Luo, L. Guang-Hong, Towards suppressing H blistering by investigating the physical origin of the H–He interaction in W, Nuclear Fusion, 50 (2010) 115010.

[35] X.T. Zu, L. Yang, F. Gao, S.M. Peng, H.L. Heinisch, X.G. Long, R.J. Kurtz, Properties of helium defects in bcc and fcc metals investigated with density functional theory, Physical Review B, 80 (2009) 054104.

[36] Y.-L. Liu, Y. Zhang, H.-B. Zhou, G.-H. Lu, F. Liu, G.N. Luo, Vacancy trapping mechanism for hydrogen bubble formation in metal, Physical Review B, 79 (2009) 172103.

[37] T. Seletskaia, Y. Osetsky, R.E. Stoller, G.M. Stocks, First-principles theory of the energetics of He defects in bcc transition metals, Physical Review B, 78 (2008) 134103.

[38] T. Seletskaia, Y. Osetsky, R.E. Stoller, G.M. Stocks, Magnetic Interactions Influence the Properties of Helium Defects in Iron, Physical review letters, 94 (2005) 046403.

[39] C.-C. Fu, F. Willaime, Ab initio study of helium in α-Fe: Dissolution, migration, and clustering with vacancies, Physical Review B, 72 (2005) 064117.

[40] D.E. Jiang, E.A. Carter, Diffusion of interstitial hydrogen into and through bcc Fe from first principles, Physical Review B, 70 (2004) 064102.

[41] Y. Tateyama, T. Ohno, Stability and clusterization of hydrogen-vacancy complexes in α-Fe: An ab initio study, Physical Review B, 67 (2003) 174105.

[42] R. Vassen, H. Trinkaus, P. Jung, Helium desorption from Fe and V by atomic diffusion and bubble migration, Physical Review B, 44 (1991) 4206-4213.

[43] R.E. Stoller, The influence of helium on microstructural evolution: Implications for DT fusion reactors, Journal of Nuclear Materials, 174 (1990) 289-310.

[44] S.R. Lee, S.M. Myers, R.G.S. Jr., Trapping of deuterium by helium bubbles and defects in ion-implanted tantalum, Journal of Applied Physics, 66 (1989) 1137-1148.

[45] E.E. Bloom, The challenge of developing structural materials for fusion power systems, Journal of Nuclear Materials, 258-263 (1998) 7-17.

[46] M.R. Gilbert, S.L. Dudarev, D. Nguyen-Manh, S. Zheng, L.W. Packer, J.C. Sublet, Neutron-induced dpa, transmutations, gas production, and helium embrittlement of fusion materials, Journal of Nuclear Materials, 442 (2013) S755-S760.

[47] J.P. Hirth, Effects of hydrogen on the properties of iron and steel, Metallurgical Transactions A, 11 (1980) 861-890.

[48] I. Takagi, K. Matsuoka, T. Tanaka, M. Akiyoshi, T. Sasaki, Hydrogen trapping in 3He-irradiated Fe, Nuclear Instruments & Methods in Physics Research Section B, 314 (2013) 117-121.

[49] Q. Xu, J. Zhang, Effects of He, D interaction on thermal desorption of He and D2 and microstructural evolution in pure Fe, Journal of Nuclear Materials, 479 (2016) 255-259.

[50] N. Hashimoto, S. Sakuraya, J. Tanimoto, S. Ohnuki, Effect of impurities on vacancy migration energy in Fe-based alloys, Journal of Nuclear Materials, 445 (2014) 224-226.

[51] Y.-L. Liu, Y. Yu, Z.-H. Dai, Statistical model and first-principles simulation on concentration of HenV cluster and He bubble formation in α-Fe and W, Journal of Nuclear Materials, 456 (2015) 162-173.

[52] J.J. Mortensen, L.B. Hansen, K.W. Jacobsen, Real-space grid implementation of the projector augmented wave method, Physical Review B, 71 (2005) 035109.

[53] J.P. Perdew, K. Burke, M. Ernzerhof, Generalized Gradient Approximation Made Simple, Physical review letters, 77 (1996) 3865-3868.

[54] H.J. Monkhorst, J.D. Pack, Special points for Brillouin-zone integrations, Physical Review B, 13 (1976) 5188-5192.

[55] M.J. Puska, R.M. Nieminen, M. Manninen, Atoms embedded in an electron gas: Immersion energies, Physical Review B, 24 (1981) 3037-3047.

[56] J.L. Fan, X. Gong, B.Y. Huang, M. Song, T. Liu, J.M. Tian, Densification behavior of nanocrystalline W–Ni–Fe composite powders prepared by sol-spray drying and hydrogen reduction process, Journal of Alloys and Compounds, 489 (2010) 188-194.

[57] R.D. Smirnov, S.I. Krasheninnikov, A.Y. Pigarov, T.D. Rognlien, Tungsten dust impact on ITER-like plasma edge, Physics of Plasmas, 22 (2015) 012506.

[58] J.-J. Pak, M. Bahgat, M.-K. Paek, Synthesis and reduction behavior of sol-precipitated iron oxide/tungsten oxide nanoparticles, Journal of Alloys and Compounds, 479 (2009) 613-618.

[59] R. Neu, H. Maier, M. Balden, S. Elgeti, H. Gietl, H. Greuner, A. Herrmann, A. Houben, V. Rohde, B. Sieglin, I. Zammuto, Investigations on tungsten heavy alloys for use as plasma facing material, Fusion Engineering and Design, 124 (2017) 450-454.

[60] S.A. Humphry-Baker, R.W. Harrison, G. Greaves, A.J. Knowles, G.D.W. Smith, S.E. Donnelly, W.E. Lee, A candidate fusion engineering material, WC-FeCr, Scripta Materialia, 155 (2018) 129-133.

[61] J. Riesch, T. Höschen, L. Ch, S. Wurster, J.H. You, Enhanced toughness and stable crack propagation in a novel tungsten fibre-reinforced tungsten composite produced by chemical vapour infiltration, Physica Scripta, 2014 (2014) 014031.

[62] A.F. Rowcliffe, L.M. Garrison, Y. Yamamoto, L. Tan, Y. Katoh, Materials challenges for the fusion nuclear science facility, Fusion Engineering and Design, 135 (2018) 290-301.

[63] J.X. Yang, L. Chen, J.L. Fan, H.R. Gong, Doping of helium at Fe/W interfaces from first principles calculation, Journal of Alloys & Compounds, 686 (2016) 160-167.

[64] M.R. Gilbert, S.L. Dudarev, S. Zheng, L.W. Packer, J.-C. Sublet, An integrated model for materials in a fusion power plant: transmutation, gas production, and helium embrittlement under neutron irradiation, Nuclear Fusion, 52 (2012) 083019.

[65] N. Yamamoto, T. Chuto, Y. Murase, J. Nagakawa, Correlation between embrittlement and bubble microstructure in helium-implanted materials, Journal of Nuclear Materials, 329-333 (2004) 993-997.

[66] H.K. Birnbaum, P. Sofronis, Hydrogen-enhanced localized plasticity—a mechanism for hydrogen-related fracture, Materials Science and Engineering: A, 176 (1994) 191-202.

[67] R.A. Oriani, P.H. Josephic, Equilibrium and kinetic studies of the hydrogen-assisted cracking of steel, Acta Metallurgica, 25 (1977) 979-988.

[68] J. Shi, N. Hashimoto, Study on synergistic effects of H and He in α-Fe, Nuclear Materials and Energy, 16 (2018) 212-216.

[69] J. Enkovaara, C. Rostgaard, J.J. Mortensen, J. Chen, M. Dułak, L. Ferrighi, J. Gavnholt, C. Glinsvad, V. Haikola, H.A. Hansen, H.H. Kristoffersen, M. Kuisma, A.H. Larsen, L. Lehtovaara, M. Ljungberg, O. Lopez-Acevedo, P.G. Moses, J. Ojanen, T. Olsen, V. Petzold, N.A. Romero, J. Stausholm-Møller, M. Strange, G.A. Tritsaris, M. Vanin, M. Walter, B. Hammer, H. Häkkinen, G.K.H. Madsen, R.M. Nieminen, J.K. Nørskov, M. Puska, T.T. Rantala, J. Schiøtz, K.S. Thygesen, K.W. Jacobsen, Electronic structure calculations with GPAW: a real-space implementation of the projector augmented-wave method, Journal of Physics: Condensed Matter, 22 (2010) 253202.

[70] W. Wulfhekel, F. Zavaliche, R. Hertel, S. Bodea, G. Steierl, G. Liu, J. Kirschner, H.P. Oepen, Growth and magnetism of Fe nanostructures on W(001), 68 (2003).

[71] H. Lee, I.-G. Baek, E. Vescovo, Spin reorientation transition in Fe-rich alloy films on W (110): The role of magnetoelastic anisotropy and structural transition, Applied physics letters, 89 (2006) 112516.

[72] H.G. Lee, I.G. Baek, S. Kim, E. Vescovo, Electronic and magnetic properties in Fe-based Fe1−xNix, Fe1−xCox, and Fe1−xVx films on W(110), Surface Science, 600 (2006) 4137-4142.

[73] P.J. Berlowitz, J.W. He, D.W. Goodman, Overlayer growth and chemisorptve properties of ultra-thin Fe films on W(110) and W(100), Surface Science, 231 (1990) 315-324.

[74] J. Chen, J.L. Erskine, Surface-step-induced magnetic anisotropy in thin epitaxial Fe films on W(001), Physical review letters, 68 (1992) 1212-1215.

[75] M. Rybicki, I. Zasada, K. Freindl, N. Spiridis, J. Korecki, A LEED study of surface relaxation in Fe(110) epitaxial film on W(110), Applied Surface Science, 286 (2013) 66-70.

[76] Q.Q. Ren, J.L. Fan, H.R. Gong, Work function and cohesion properties of W–Fe interfaces, Materials Letters, 145 (2015) 205-208.

[77] L. Dubrovinsky, S.J.P. Saxena, C.o. Minerals, Thermal expansion of periclase (MgO) and tungsten (W) to melting temperatures, 24 (1997) 547-550.

[78] D.F. Johnson, E.A. Carter, Hydrogen in tungsten: Absorption, diffusion, vacancy trapping, and decohesion, Journal of Materials Research, 25 (2010) 315-327.

[79] X. Qian, W. Hübner, Symmetry and substrate effects on magnetic interactions from first principles: A comparison between Fe/W(100) and Fe/W(110), Physical Review B, 67 (2003) 184414.

[80] M. Shin, B.-G. Park, C. Hwang, H. Lee, Correlation between ferromagnetic state and thermally stable layer of Fe on the W(001) surface, Current Applied Physics, 14 (2014) 68-71.

[81] S. Bagchi, S. Jani, S. Anwar, N. Lakshmi, N.P. Lalla, Structural and magnetic study of swift heavy ion irradiated W/Fe multilayer structure, Journal of Magnetism and Magnetic Materials, 322 (2010) 3851-3856.

[82] M. Heide, G. Bihlmayer, S. Blügel, Dzyaloshinskii-Moriya interaction accounting for the orientation of magnetic domains in ultrathin films: Fe/W(110), Physical Review B, 78 (2008).

[83] J. Kołaczkiewicz, E. Bauer, V and Fe on the W(110) face, Surface Science, 450 (2000) 106-116.

[84] O. Fruchart, J.P. Nozières, D. Givord, Growth and interface magnetic anisotropy of epitaxial Mo/Fe/Mo(110) and W/Fe/W(110) ultrathin films, Journal of Magnetism and Magnetic Materials, 207 (1999) 158-167.

[85] E.D. Tober, R.X. Ynzunza, F.J. Palomares, Z. Wang, Z. Hussain, M.A. Van Hove, C.S. Fadley, Interface Structures of Ordered Fe and Gd Overlayers on W(110) from Photoelectron Diffraction, Physical review letters, 79 (1997) 2085-2088.

[86] M. Przybylski, U. Gradmann, J. Korecki, Magnetic hyperfine fields near the

W(110)/Fe(110)-interface, Journal of Magnetism and Magnetic Materials, 69 (1987) 199-205.

[87] H. Bethge, D. Heuer, C. Jensen, K. Reshöft, U. Köhler, Misfit-related effects in the epitaxial growth of iron on W(110), Surface Science, 331-333 (1995) 878-884.

[88] I. Galanakis, M. Alouani, H. Dreyssé, Interface magnetism in ultrathin Fe/W(110) films from first principles, Physical Review B, 62 (2000) 3923-3928.

[89] J.W. Coenen, S. Antusch, M. Aumann, W. Biel, J. Du, J. Engels, S. Heuer, A. Houben, T. Hoeschen, B. Jasper, F. Koch, J. Linke, A. Litnovsky, Y. Mao, R. Neu, G. Pintsuk, J. Riesch, M. Rasinski, J. Reiser, M. Rieth, A. Terra, B. Unterberg, T. Weber, T. Wegener, J.H. You, C. Linsmeier, Materials for DEMO and reactor applications—boundary conditions and new concepts, Physica Scripta, T167 (2015) 014002.

[90] M.J. Demkowicz, R.G. Hoagland, J.P. Hirth, Interface Structure and Radiation Damage Resistance in Cu-Nb Multilayer Nanocomposites, Physical review letters, 100 (2008) 136102.

[91] S. Heuer, J. Matějíček, M. Vilémová, M. Koller, K. Illkova, J. Veverka, T. Weber, G. Pintsuk, J.W. Coenen, C. Linsmeier, Atmospheric plasma spraying of functionally graded steel/tungsten layers for the first wall of future fusion reactors, Surface and Coatings Technology, 366 (2019) 170-178.

[92] S. Heuer, T. Lienig, A. Mohr, T. Weber, G. Pintsuk, J.W. Coenen, F. Gormann, W. Theisen, C. Linsmeier, Ultra-fast sintered functionally graded Fe/W composites for the first wall of future fusion reactors, Composites Part B: Engineering, 164 (2019) 205-214.

[93] W. Tang, E. Sanville, G. Henkelman, A grid-based Bader analysis algorithm without lattice bias, Journal of Physics: Condensed Matter, 21 (2009) 084204.

[94] M. Yu, D.R. Trinkle, Accurate and efficient algorithm for Bader charge integration, The Journal of chemical physics, 134 (2011) 064111.

[95] E. Sanville, S.D. Kenny, R. Smith, G. Henkelman, Improved grid-based algorithm for Bader charge allocation, Journal of computational chemistry, 28 (2007) 899-908.

[96] X. Qian, W. Hübner, Ab initio magnetocrystalline anisotropy calculations for Fe/W(110) and Fe/Mo(110), Physical Review B, 64 (2001) 092402.

[97] P. Söderlind, L.H. Yang, J.A. Moriarty, J.M. Wills, First-principles formation energies of monovacancies in bcc transition metals, Physical Review B, 61 (2000) 2579-2586.

Achievements

- 2016/12 JIM Hokkaido branch winter meeting, Oral presentation
- 2017/11 The 18th International Conference on Fusion Reactor Materials, Poster
- 2018/01 JIM Hokkaido branch 2018 winter meeting, Oral presentation
- 2018/03 JIM 2018 Annual Spring Meeting, Oral presentation
- 2018/09 JIM 2018 Annual Fall Meeting, Oral presentation
- 2018/09 Japan-China Symposium on Materials for Advanced Energy Systems and Fission & Fusion Engineering, Poster
- 2018/10 The Nuclear Materials Conference 2018, Oral presentation
- 2018/12 JIM Hokkaido branch 2019 winter meeting, Oral presentation
- 2019/10 The 18th International Conference on Fusion Reactor Materials, Poster